Pergamon

Int. J. Heat Mass Transfer. Vol. 39, No. 3, pp. 575–601, 1996

0017-9310/96 $9.50+0.00

0017-9310(95)00073-9

Solid-propellant fire in an enclosure fitted with a ceiling safety-vent

B. PORTERIE, M. LARINI, F. GIROUD and J.-C. LORAUD

Département Ecoulements Diphasiques et Réactifs, IUSTI, UMR CNRS 139,
Université de Provence, Marseille, France

(*Received* 10 *February* 1994 *and in final form* 27 *January* 1995)

Abstract—The response of an enclosure having a ceiling safety-vent to a fire of solid propellant located on the floor is investigated numerically. The full Navier–Stokes equations are solved along with the species continuity equations. A recent method is used to compute chemical equilibria and the coupling between chemistry and thermodynamics is treated according to a new strategy. The particular boundaries, which are the combustion zone of the propellant and the outflow section, require an original treatment by solving a set of 'full' or 'half' Riemann problems taking into account the transport of chemical species. The SOLA-ICE algorithm is successfully developed for the reactive–diffusive case dealing with particular boundaries. A fire of a standard hot homogeneous propellant in a rectangular cavity initially filled with air is simulated for two opening conditions of the safety-vent. They predict the increase in the rates of energy release and CO_2/H_2O production in the reaction zone caused by afterburning processes involving the air of the enclosure. The course of the compartment fire is described in terms of time evolution of the average gas temperature and pressure, and oxygen depletion for both opening configurations.

1. INTRODUCTION

The flow motion induced by fires in confined space is of widespread interest in fire safety. The elaboration of efficient methods of fire detection and control yields the need for a full understanding of these flows. Thus, a large number of experimental and numerical studies have been devoted to enclosure fires. The reader is referred to ref. [1] for overall descriptions of compartment fire phenomena and some relevant experimental works. A comprehensive review of the available mathematical models is given by Mitler [2]; zone models (see for example refs. [3–7]) and field models (see for example refs. [8–9]).

Severe fire accidents may occur in facilities (such as military stores, holds of ships and submarines) where active substances, such as solid propellant, are stored. Recent fires that occured on USS Stark in the Persian Gulf in 1987 [10] or on surface vessels during the war of the Falkland Islands have demonstrated the danger of the uncontrolled combustion of such materials. That has motivated research activities to model combustion processes in these facilities in order to define well-adapted fire-safety requirements [11–14].

Solid propellants are materials able to generate exothermic reactions without the addition of any other reactants. Their characteristic feature is that the fuel and oxidizer are initially intimately mixed in order to provide self-sustained combustion. There are two types of propellants which are distinguished by the condition in which their ingredients are connected. Homogeneous propellants consist of a substance in which oxidizer and fuel are linked chemically in their structure and heterogeneous propellants consist in two substances, as an oxidizer and a fuel, which are physically mixed. This study is devoted to homogeneous (double-base) propellant combustion. Homogeneous propellants are often used in anti-tank rockets or missiles and in some tactical missiles because of their smokeless properties. From the works reported in refs. [15–23], in particular the work of Lengelle *et al.* [17], it is possible to describe briefly the general behavior and the flame structure of homogeneous propellants. As illustrated in Fig. 1, from ref. [17], in the subsurface reaction zone, initial C—O—//—NO_2 bond breaking is followed by secondary recombination reactions. A mixture of NO_2, aldehydes, and NO emerges from the surface. In the gas phase, at low pressure, a three-zone flame structure may be observed: (i) a nonluminous primary flame zone ('fizz zone') which begins at the surface and is quite thin (about 200 μm at 1 atm [22]), (ii) an induction zone ('dark zone') which is very thick at low pressure, and (iii) a secondary luminous flame which is a thin reaction zone where the final combustion gases are produced. In the fizz zone, the NO_2 is partially reduced to NO by reactions with aldehydes while, in the secondary flame, the NO is reduced to N_2. With increasing pressure, the dark zone collapses and the two flames merge into one overall flame at the regressing propellant surface. The final combustion products in the secondary flame are CO, CO_2, H_2, H_2O, O_2 and N_2. These products are under-oxidized (high CO, H_2), and, if combustion takes place in air, afterburning reactions occur leading to a significant increase of energy and production of CO_2 and H_2O.

Qualitative and quantitative information con-

NOMENCLATURE

C_p	constant-pressure specific heat
D_{sm}	diffusion coefficient of species s in the mixture
D_{sv}	binary diffusion coefficient
e	specific internal energy
g	gravitational acceleration
h	enthalpy
k	thermal conductivity
M	molecular weight
N	number of species of the mixture
n	number of moles
p	pressure
R	universal gas constant
s	entropy
T	temperature
T_0	fixed standard reference temperature
u, v	components of the mass-average velocity of the mixture in the x and y directions
V_{sx}, V_{sy}	components of the mass diffusion velocity of species s in the x and y directions
X	mole fraction
Y	mass fraction.

Greek symbols

Δh_{fs}^0	heat of formation of species s
μ	dynamic viscosity
ρ	density
ω_s	mass rate of production of species s.

Subscripts

s, v	sth and vth species
r, r^*, l, l^*	right and left states in a Riemann problem.

cerning propellant combustion are generally based on experiments from strand burners which are pressurized with inert gas (nitrogen) and the pressure is seldom lower than 10 atm. Fifer [22] indicates that below about 15 atm many propellants burn without a secondary flame. During such 'fizzing burning', no flame is visible and the combustion products reflect the incomplete burning of the fizz zone. Therefore, when the propellant burns at atmospheric pressure, it seems reasonable to assume that the contribution of the NO reduction reaction is not very significant. This assumption is made in this work which is concerned with the numerical study of the flowfield induced by a solid-propellant fire in an enclosure. Emphasis is put on dynamic aspects of the flow.

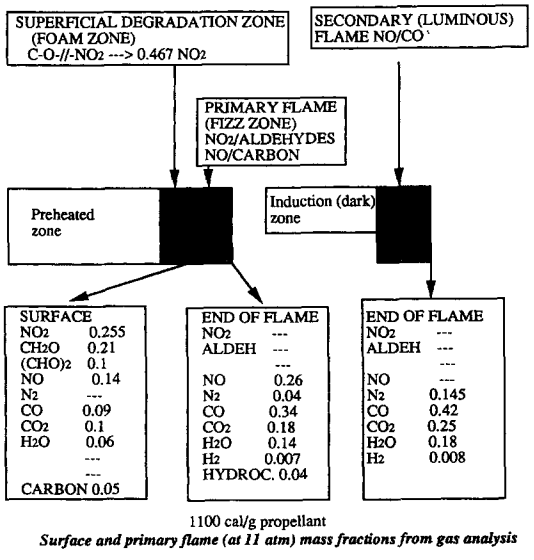

Fig. 1. Various zones in the combustion of a double-base propellant.

The enclosure is initially filled with air at atmospheric pressure. The combustible material is located on the floor of the cavity and a ceiling safety-vent is used for venting the pressurized enclosure. The thinness of the fizz zone compared with the dimensions of the rectangular cavity (2 m × 1 m) allows us to model the propellant combustion as a generation of gases identical to those evolved at the end of the primary flame (same temperature and composition). As described previously, afterburning reactions occur with the surrounding air involving CO–O_2 and H_2-O_2 reactions.

A good description of afterburning processes requires accounting for chemical reactions and mass diffusion, the flow in the enclosure is described by the reactive–diffusive Navier–Stokes equations.

To describe the combustion of a weakly sooting mixture, chemical equilibrium may be assumed. Real-gas chemistry is coupled to the conservation equations by way of an equilibrium chemistry package. This package is based on the recent method of Heuzé *et al.* [24] for the equilibrium computation of the gaseous mixture.

For the complex boundaries that are the floor combustion zone and the ceiling inflow/outflow opening, an original treatment is proposed. At each point of these boundaries, conditions are determined by solving a one-dimensional reactive Riemann problem.

The SOLA-ICE algorithm, which is a variation of the ICE (Implicit Continuous-fluid Eulerian) method developed by Harlow and Amsden [25], has been extended to reactive flow.

In Section 2, a detailed description of the mathematical model is given. Section 3 describes the

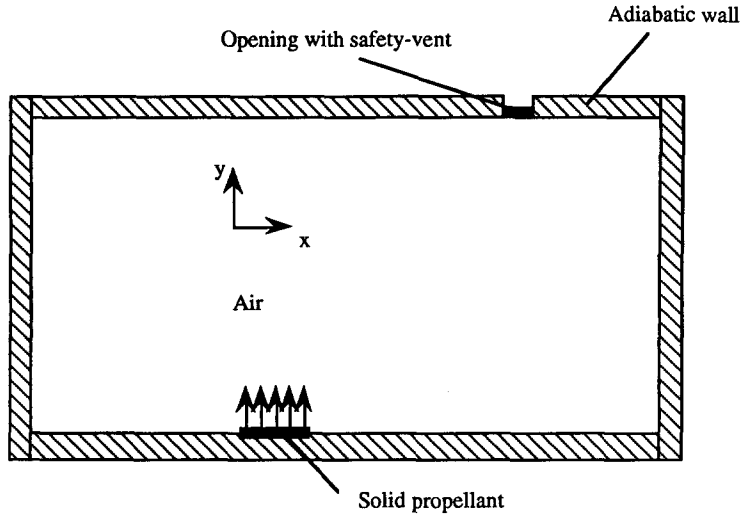

Fig. 2. Physical model of enclosure.

numerical technique, and the results are discussed in detail in Section 4. Finally, conclusions are given in Section 5.

2. ANALYSIS

Physical model

The model used for this study is illustrated in Fig. 2.

The two-dimensional rectangular enclosure is surrounded by adiabatic walls. Initially, the enclosed air and the walls are at ambient temperature and the air is stagnant. The enclosure has a venting system closed by a safety-vent designed to prevent overpressure. At time $t > 0$ and some arbitrary (specified) location on the floor, a slab of solid propellant ignites. The hot gases produced by combustion expand, rise and get in contact with the air by convection and mass-diffusion. In the mixing region of the hot gas and air streams, afterburning reaction can occur. As long as the enclosure is hermetically sealed, the pressure and temperature of the internal flow increase significantly. Once the assigned bursting pressure of the safety-vent is attained, the hot gases escape from the compartment. Next, external cool air inflow can occur due to a possible pressure drop in the enclosure.

The basic assumptions made in the analysis are as follows.

(i) The unsteady flow is assumed to be laminar and two-dimensional.

(ii) Dufour effect is negligible.

(iii) Radiation effects are neglected.

(iv) Departures from local chemical equilibrium are negligible.

(v) Once the enclosure is vented, the flow escapes vertically from the compartment to an outside region which contains stagnant air at atmospheric pressure and ambient temperature.

(vi) The gaseous products of propellant combustion are generated vertically.

Diffusion and viscous dissipation effects, and dependence of transport properties on temperature (and pressure, eventually) are included in this work. Full compressibility is allowed.

Governing equations

The governing equations of a multicomponent reacting system can be given as conservation equations written in a rectangular coordinate system (see Kuo [26]):

Equation of continuity.

$$\frac{\partial \rho}{\partial t} + \frac{\partial \rho u}{\partial x} + \frac{\partial \rho v}{\partial y} = 0 \tag{1}$$

Equation of continuity for sth species ($1 \leqslant s \leqslant N$).

$$\rho\left(\frac{\partial Y_s}{\partial t} + u\frac{\partial Y_s}{\partial x} + v\frac{\partial Y_s}{\partial y}\right) + \frac{\partial}{\partial x}(\rho Y_s V_{sx}) + \frac{\partial}{\partial y}(\rho Y_s V_{sy}) = \omega_s \tag{2}$$

where, according to Fick's law of mass diffusion

$$V_{sx} = -\frac{D_{sm}}{Y_s}\frac{\partial Y_s}{\partial x} \quad V_{sy} = -\frac{D_{sm}}{Y_s}\frac{\partial Y_s}{\partial y}.$$

For a mixture of N species, there are N equations of this kind. The sum of these equations gives equation (1). Also, any one of the species continuity equations can be replaced by

$$\sum_{s=1}^{N} Y_s = 1.$$

Equations of motion.

x component,

$$\rho\frac{\partial u}{\partial t} + \rho u\frac{\partial u}{\partial x} + \rho v\frac{\partial u}{\partial y} = -\frac{\partial p}{\partial x} + \frac{\partial \tau_{xx}}{\partial x} + \frac{\partial \tau_{yx}}{\partial y} \tag{3}$$

y component,

$$\rho\frac{\partial v}{\partial t}+\rho u\frac{\partial v}{\partial x}+\rho v\frac{\partial v}{\partial y}=-\rho g-\frac{\partial p}{\partial y}+\frac{\partial \tau_{yy}}{\partial y}+\frac{\partial \tau_{xy}}{\partial x} \quad (4)$$

$$\begin{cases}\tau_{xx}=\frac{2}{3}\mu\left(2\dfrac{\partial u}{\partial x}-\dfrac{\partial v}{\partial y}\right)\\ \tau_{yy}=\frac{2}{3}\mu\left(-\dfrac{\partial u}{\partial x}+2\dfrac{\partial v}{\partial y}\right)\\ \tau_{xy}=\tau_{yx}=\mu\left(\dfrac{\partial u}{\partial y}+\dfrac{\partial v}{\partial x}\right).\end{cases}$$

Energy equation. Neglecting the radiation effects and the Dufour effect contribution to the heat flux, it follows that

$$\rho\left(\frac{\partial e}{\partial t}+u\frac{\partial e}{\partial x}+v\frac{\partial e}{\partial y}\right)$$

$$=-p\left(\frac{\partial u}{\partial x}+\frac{\partial v}{\partial y}\right)-\frac{\partial q_x}{\partial x}-\frac{\partial q_y}{\partial y}$$

$$+\tau_{xx}\frac{\partial u}{\partial x}+\tau_{yx}\frac{\partial v}{\partial x}+\tau_{xy}\frac{\partial u}{\partial y}+\tau_{yy}\frac{\partial v}{\partial y} \quad (5)$$

where the specific internal energy is defined to include the chemical energy

$$e=\sum_{s=1}^{N}Y_s h_s-\frac{p}{\rho} \quad (6)$$

and

$$q_x=-k\frac{\partial T}{\partial x}+\rho\sum_{s=1}^{N}h_s Y_s V_{sx}$$

$$q_y=-k\frac{\partial T}{\partial y}+\rho\sum_{s=1}^{N}h_s Y_s V_{sy}$$

where

$$h_s=\Delta h_{fs}^0+\int_{T_0}^{T}C_{ps}\,\mathrm{d}T.$$

In equation (6), the constant-pressure specific heat of each species is deduced from a fifth-order polynomial in temperature [27].

The equation of state for a multicomponent system based upon ideal-gas assumptions can be written as

$$p=\rho RT\sum_{s=1}^{N}\frac{Y_s}{M_s}. \quad (7)$$

Evaluation of mixture viscosity, conductivity, and diffusion coefficients. The computer code package developed by Kee *et al.* [28] is used in conjunction with the CHEMKIN code [29] for the evaluation of the transport properties of each pure species. It computes third-order polynomial fits of the logarithm of the property vs the logarithm of the temperature.

The average mixture viscosity is deduced from the pure species viscosities μ_s according to the semi-empirical formula of Wilke [30]:

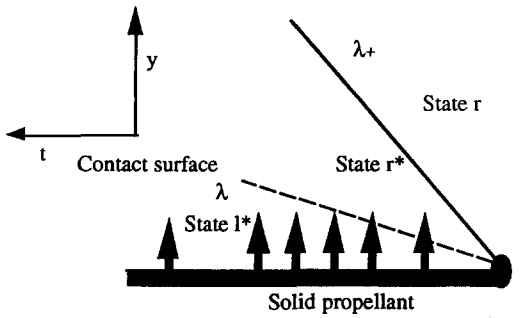

Fig. 3. Riemann problem at the surface of the solid propellant.

$$\mu=\sum_{s=1}^{N}\frac{X_s\mu_s}{\sum_{v=1}^{N}X_v\phi_{sv}}$$

where

$$\phi_{sv}=\frac{1}{\sqrt{8}}\left(1+\frac{M_s}{M_v}\right)^{-1/2}\left[1+\left(\frac{\mu_s}{\mu_v}\right)^{1/2}\left(\frac{M_v}{M_s}\right)^{1/4}\right]^2.$$

A similar formula is used to determine the mixture conductivity.

We determine the diffusion coefficient of the species s in the mixture by the following formula [28]:

$$D_{sm}=\frac{\sum_{v\neq s}^{N}X_v M_v}{M\sum_{v\neq s}^{N}\dfrac{X_v}{D_{sv}}}.$$

Boundary conditions

Three types of boundaries must be dealt with.

— Solid boundaries defined by the cavity walls (including the safety-vent until it opens). The no-slip condition for velocity components and a zero value for the normal gradients of density, internal energy (which is equivalent to the adiabatic condition), and species mass-fractions are imposed.

— The boundary defined by the combustion zone of the propellant considered as a gaseous product-generating zone at floor level. Flow parameters at this level are obtained by solving at each point a 'half' Riemann problem.

— The boundary defined by the ceiling opening after diaphragm burst. A 'full' Rieman problem is solved at each point.

Propellant combustion gaseous products-generating zone. The combustion gaseous products are supposed to be generated normally to the surface of the propellant slab. Their state is l^*, for which the temperature $T=T_{l^*}$, the cross-section mass flow rate $\dot{m}=\rho_{l^*}v_{l^*}$ and the chemical equilibrium composition $Y_s=Y_{sl^*}$, $s=1,2,\ldots,N$ are given (fizz zone products).

As shown in Fig. 3, each point of the surface generates two elementary waves: the λ^+ wave of slope $u+a$ and the λ wave of slope u. Across these waves,

some parameters remain constant: these are the Riemann invariants.

A 'half' Riemann problem is solved at each boundary point.

Knowledge of the limit values and of the state r of the interior point computed at the previous time step yields the state l^*. By using the Riemann invariants the states r and r^* may be linked across the λ^+ wave according to the equation (see Appendix)

$$v_r = v_{r^*} - 2\left[\frac{1}{Z_r}(Z_r+1)(e_r-q_r)\right]^{1/2} \times \left[\left(\frac{p_{r^*}}{p_r}\right)^{[Z_r/2(Z_r+1)]} - 1\right] \quad \text{(A4)}$$

and across the λ wave

$$v_{r^*} = v_{l^*}, p_{r^*} = p_{l^*} \quad (8)$$

with

$$v_{l^*} = \frac{\dot{m}}{\rho_{l^*}} \quad (9)$$

and

$$p_{l^*} = \rho_{l^*} R T_{l^*} \sum_{s=1}^{N} \frac{Y_{sl^*}}{M_s} \quad (10)$$

where Z_r is given by equation (A1) in the Appendix. Equations (8)–(10) are combined in order to eliminate v_{r^*} in equation (A4) which becomes

$$v_r - \frac{\dot{m} R T_{l^*} \sum_{s=1}^{N} \frac{Y_{sl^*}}{M_s}}{p_{r^*}} + 2\left[\frac{1}{Z_r}(Z_r+1)(e_r-q_r)\right]^{1/2} \times \left[\left(\frac{p_{r^*}}{p_r}\right)^{[Z_r/2(Z_r+1)]} - 1\right] = 0. \quad (11)$$

Knowing $\dot{m}$, T_{l^*} and $Y_s = Y_{sl^*}$, $s = 1, 2, \ldots, N$, the pressure p_{r^*} is then obtained from equation (11) by an iterative procedure, then v_{r^*} from (A4), and ρ_{l^*} from (9).

The internal energy e_{l^*} is given by (6).

Opening zone. The gas flow is supposed to be normal to the outlet cross-section. We must solve a 'full' Riemann problem at each point of this boundary, from which three elementary waves are issued: the λ^+ wave of slope $u+a$, the λ^- wave of slope $u-a$ and the λ wave of slope u (Fig. 4). In this case the problem is to determine the l^* and r^* states knowing the r and l states. In our case, as the fluid outside the cavity is ambient still air, the state r has been completely determined, the interior point state l being computed at the previous time step.

Two flow configurations are possible, as the fluid flows either out of or into the cavity. In the first case, the fluid will be in state l^* at the outlet section (Fig. 4(a)). In the second case, the fluid will be in state r at the outlet section (Fig. 4(b)).

Taking into account the Riemann invariants across the λ^+, λ^- and λ waves, the different states r, r^*, l, l^* are linked by the following conditions (see Appendix)

$$v_l - 2\left[\frac{1}{Z_l}(Z_l+1)(e_l-q_l)\right]^{1/2}\left[\left(\frac{p_{l^*}}{p_l}\right)^{[Z_l/2(Z_l+1)]} - 1\right] = v_r + 2\left[\frac{1}{Z_r}(Z_r+1)(e_r-q_r)\right]^{1/2} \left[\left(\frac{p_{r^*}}{p_r}\right)^{[Z_r/2(Z_r+1)]} - 1\right] \quad (12)$$

$$v_{r^*} = v_{l^*} \quad (13)$$

$$p_{r^*} = p_{l^*}. \quad (14)$$

Equation (12) is obtained from (A4) and (A5). Using equation (12) and considering equation (14), the outlet pressure may be obtained by an iterative procedure. Velocity is obtained from (A4) or (A5).

The temperature, mass fractions and the internal energy at the outlet section may now be determined.

If the flow is directed outwards, then the gas at the outlet section will be in the l^* state. The gas composition is obtained from:

$$Y_{sl^*} = Y_{sl} \quad s = 1, 2, \ldots, N$$

as Y_s is a Riemann invariant across the λ wave. Usually it consists of combustion gases mixed with residual air.

Using the isentropic relations (A7) between the l and l^* states, we have:

$$\rho_{l^*} = \rho_l\left(\frac{p_{l^*}}{p_l}\right)^{1/(Z_l+1)}$$

$$e_{l^*} = q_l + (e_l - q_l)\left(\frac{p_{l^*}}{p_l}\right)^{Z_l/(Z_l+1)}.$$

If the flow is directed inwards, then the gas at the outlet section will be in the r^* state. The gas composition is given by:

$$Y_{sr^*} = Y_{sr} \quad s = 1, 2, \ldots, N$$

as Y_s is a Riemann invariant across the λ_+ wave. It is the ambient fresh air which enters the cavity. Using the isentropic relations (A7) between the r and r^* states, we have:

$$\rho_{r^*} = \rho_r\left(\frac{p_{r^*}}{p_r}\right)^{1/(Z_r+1)}$$

$$e_{r^*} = q_r + (e_r - q_r)\left(\frac{p_{r^*}}{p_r}\right)^{Z_r/(Z_r+1)}.$$

The temperature is in both cases determined using the equation of state.

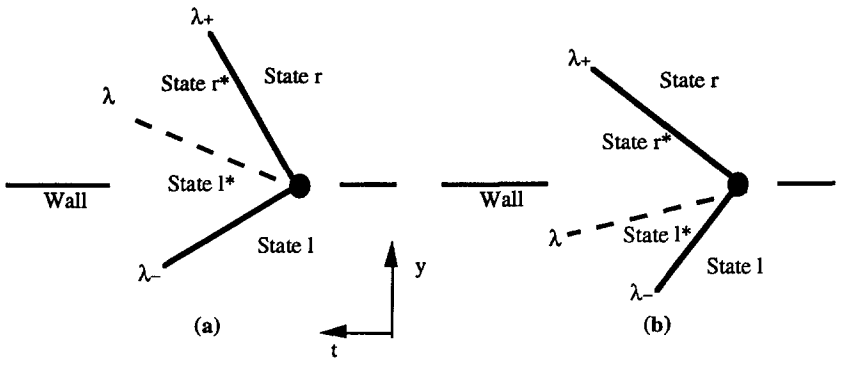

Fig. 4. Riemann problems at the ceiling opening.

Reactive model

Fire is the result of the coupling between dynamic phenomena (convection, chemical species diffusion) and a reactive mechanism occuring in each point any time when the reactive species are brought in contact and thermodynamic conditions are favorable. When the reactive and the oxydant are initially separated, combustion may only occur at the points where molecular diffusion has been able to mix them. This approach implies the use of the mathematical model discussed above, since without species diffusion the reactive processes cannot take place.

In the present model, up to seven chemical species are involved: CO, CO_2, H_2, H_2O, O_2, NO (inert) and N_2 (inert). Dissociation of H_2, O_2 and N_2 is not considered.

Considering the assumption of chemical equilibrium, the composition of the mixture is calculated for assigned thermodynamic states by specifying the pressure and temperature.

The equilibrium composition of a gaseous mixture is generally determined using the equilibrium constant formulation or the Gibbs free-energy minimization procedure. The latter is well suited for computer calculations. In the present work, the minimization is performed using the method developed by Heuzé *et al.* [24]. In this method, the chemical equilibrium is obtained once the chemical affinity of each equilibrium reaction is zero. It leads to a fast convergence and provides good accuracy for components that appear in small amounts.

A particular problem which had to be dealt with when coupling chemical equilibrium to flow computation is related to the fact that chemical composition may be very different from point to point. In fact the composition at a given time is the consequence of the initial conditions, of the dynamic convection phenomena, of the molecular diffusion and chemical reactions which occurred some instants before. For example, in one point of the flowfield, air may be the only component, while in another point all the species may be present. In the latter case the concentrations may be very different from one point to another since some chemical species may be predominant or just as traces. This implies the use of different chemical equilibrium computing strategies for each point of the flowfield according to the chemical species present and their concentrations. The means for solving this problem are discussed at the end of this section.

Computation of an equilibrium mixture composition. To better understand the global chemical strategy of our computer code, the mathematical formulation of the method of Heuzé *et al.* is briefly reviewed below through an example (see ref. [24] for the detailed method).

Let us consider a gaseous mixture in which all the components given previously are present: CO, CO_2, H_2, H_2O, O_2 NO and N_2. Since NO and N_2 are assumed to be chemically inert, only the first five components are considered in the calculation procedure. Here, $n = 5$ is the number of components based on $m = 3$ atomic species (C, H, O). The m mass balance equations of the atomic species are

$$\begin{aligned} d_C &= n_{CO} + n_{CO_2} \\ d_H &= 2n_{H_2} + 2n_{H_2O} \\ d_O &= n_{CO} + 2n_{CO_2} + n_{H_2O} + 2n_{O_2}. \end{aligned} \tag{15}$$

The n components are split into two parts, m 'basic' and $(n-m)$ 'non-basic' components. Hereafter, subscripts 0 and 1 indicate 'basic' and 'non-basic' quantities respectively. Among the eight possibilities to select three 'basic' components out of five, let us take the case where the 'basic' components are CO_2, H_2O, H_2. The 'non-basic' components are CO and O_2.

Equation (15) can be written in the form

$$\mathbf{D} = \mathbf{A}_0^t \mathbf{N}_0 + \mathbf{A}_1^t \mathbf{N}_1 \tag{16}$$

where

$$\mathbf{A}_0 = \begin{bmatrix} 1 & 0 & 2 \\ 0 & 2 & 1 \\ 0 & 2 & 0 \end{bmatrix} \quad \mathbf{A}_1 = \begin{bmatrix} 1 & 0 & 1 \\ 0 & 0 & 2 \end{bmatrix}$$

$$\mathbf{N}_0 = \begin{bmatrix} n_{CO_2} \\ n_{H_2O} \\ n_{H_2} \end{bmatrix} \quad \mathbf{N}_1 = \begin{bmatrix} n_{CO} \\ n_{O_2} \end{bmatrix}.$$

To these $m = 3$ mass balance equations, $(n-m) = 2$ equations must be added to close the system. They can be obtained through the chemical affinity of $(n-m) = 2$ equilibrium reactions. They lie in expressing the 'non-basic' components as a function of the 'basic' components

$$CO = CO_2 + H_2 - H_2O \quad \text{(water-gas reaction)} \quad (17a)$$

$$O_2 = 2H_2O - 2H_2. \quad (17b)$$

The respective chemical affinities of these reactions are defined by

$$AFF_1 = \mu_{CO} - (\mu_{CO_2} + \mu_{H_2} - \mu_{H_2O}) \quad (18a)$$

$$AFF_2 = \mu_{O_2} - (2\mu_{H_2O} - 2\mu_{H_2}) \quad (18b)$$

where μ_i is the chemical potential of ith species expressed, for the special case of the ideal gas, by

$$\mu_i = G_i^0 + RT\log(P) + RT\log\left(n_i \Big/ \sum_{i=1}^{N} n_i\right) \quad (19)$$

P is the pressure expressed in atmosphere, G_i^0 the Gibbs free energy which is tabulated as a function of temperature [31].

Equation (16) may be written:

$$\mathbf{N}_0 = (\mathbf{A}_0^t)^{-1}(\mathbf{D} - \mathbf{A}_1^t\mathbf{N}_1). \quad (20)$$

Equations (18) may be written in the vectorial formulation:

$$\mathbf{AFF} = \mathbf{G}_1 - \mathbf{Z}\mathbf{G}_0 \quad (21)$$

AFF is the affinity vector for the reactions related to 'non-basic' species, $\mathbf{G}_1$ is the chemical potential vector for the 'non-basic' species and $\mathbf{G}_0$ for the 'basic' species. It is easy to show that $\mathbf{Z} = \mathbf{A}_1\mathbf{A}_0^{-1}$.

The numerical method is based upon the iterative solving of equations (20) and (21) until the **AFF** vector becomes null.

1. Starting from the mass fractions obtained by solving the general equations the **D** vector is computed.
2. The matrices $\mathbf{A}_0$ and $\mathbf{A}_1$ are computed.
3. $\mathbf{A}_0^t$, $(\mathbf{A}_0^t)^{-1}$, $\mathbf{A}_1^t$, $\mathbf{Z}$ and $\mathbf{Z}^t$ are computed.
4. The vector $\mathbf{N}_1$ is initialized and the vector $\mathbf{N}_0$ is computed according to equation (20).
5. Start of the iterative process:

(a) computation of the total number of moles,
(b) computation of $\mathbf{G}_0$, $\mathbf{G}_1$ and of **AFF** using (21),
(c) computation of the components of the new $\mathbf{N}_1$ using the empirical formula:

$$n_j^{p+1} = n_j^p \exp\left(-\frac{AFF_j}{\alpha}\right) j = 1, \ldots, (n-m)$$

where p is the iteration number and α a convergence acceleration parameter.

6. Computation of the new $\mathbf{N}_0$ using (20).

Dynamics-chemistry coupling

The coupling between the dynamic equations (1)–(5) and the chemical processes is achieved by means of the species production terms, ω_s, due to the chemical reactions in equation (2). They are computed from the concentration variation of the chemical species being considered because of the chemical equilibrium displacements.

As pointed out, the chemical species and their concentration are directly influenced by the coupling of dynamics with chemistry phenomena, hence the differences from one point to another. This prompts the elaboration of a computing strategy for the chemical production terms, a unique choice (atomic elements, 'basic' species, initial conditions, acceleration parameter) being impossible. Thus the survey of multiple possible cases along with failure tests becomes mandatory in order to direct the computation towards the other cases that are considered.

It is obvious that a distinction should be made between the cases when at some point at a given time there are no carbon atoms, no hydrogen atoms or all the species are present. These are the only cases left if hydrogen, oxygen and nitrogen dissociation is neglected. However, splitting into these three cases is not satisfactory, as at some point, at a given time, for a given set of 'basic' species and initial conditions of the $\mathbf{N}_1$ vector, a failure may still occur in the computation process. A failure is assumed if either a negative number of moles or a bad convergence of the equilibrium computation occurs. In any of these cases the choice of the 'basic' species is modified and the equilibrium computation is restarted.

Thus, for the first two cases, the three possible choices of two out of three active species of the mixture have been taken into account. For the third case there are eight possible choices. Later on it became apparent that not all the possible choices were used by the algorithm and that if two choices both lead to a success, then the results are identical.

3. NUMERICAL METHOD

The numerical solution technique chosen to solve the governing equations is based upon the SOLA-ICE algorithm [32] which is a modified version of the implicit continuous-fluid Eulerian (ICE) method developed by Harlow and Amsden [25] for transient, arbitrarily compressible flows.

The spatial discretization makes use of the staggered marker-and-cell (MAC) mesh (Fig. 5). In this mesh, the pressure, density, internal energy and mass fractions are defined at the nodes of the mesh. The horizontal component u of the velocity is defined at the middle point of the vertical side, and the vertical component v of the velocity is defined at the middle point of the horizontal side. When the staggered MAC mesh is used, a boundary Γ of the computational domain is located as shown in Fig. 5. The main advan-

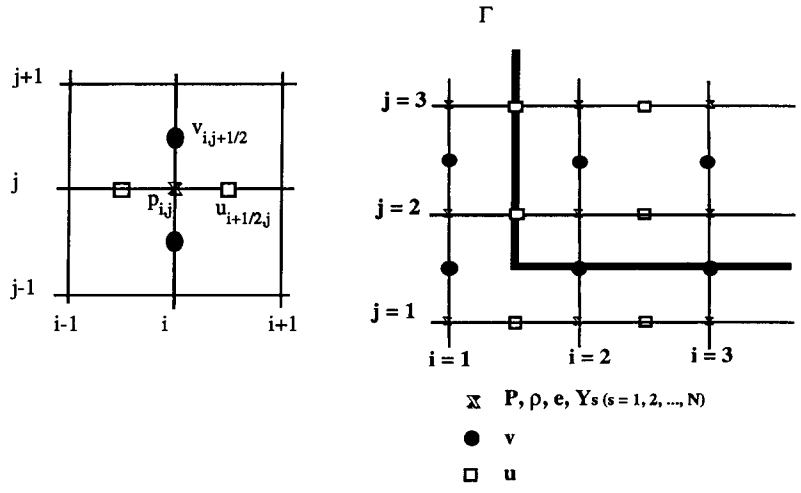

Fig. 5. The MAC mesh.

tage of such a mesh is the fact that the pressure is not defined on the boundary; this fact is essential.

In a recent paper [33], the original algorithm has been used for solving the equations governing a transient compressible one-component gas flow. In the present paper, this algorithm is extended to transient compressible multicomponent reacting flow. The basic philosophy is retained, but several modifications are necessary. They include the addition of the $N-1$ species continuity equations and the addition of mass diffusion and chemical terms in the equations. The dependence of the viscosity, thermal conductivity and diffusion coefficient on the temperature, chemical composition and eventually pressure has to be taken into account. The difference equations are then noticeably modified. For example, the x-momentum difference equation becomes

$$\frac{u_{i+1/2,j}-u^n_{i+1/2,j}}{\Delta t}+FUX+FUY$$
$$=-\frac{2}{\Delta x}\frac{\bar p_{i+1,j}-\bar p_{ij}}{\rho^n_{i+1,j}+\rho^n_{ij}}+\frac{2}{(\rho^n_{i+1,j}+\rho^n_{ij})}$$
$$\times\left\{\frac{1}{\Delta x}[(\tau_{xx})^n_{i+1,j}-(\tau_{xx})^n_{ij}]\right.$$
$$\left.+\frac{1}{\Delta y}[(\tau_{xy})^n_{i+1/2,j+1/2}-(\tau_{xy})^n_{i+1/2,j-1/2}]\right\} \qquad (22)$$

where

$$FUX=\left(u\frac{\partial u}{\partial x}\right)^n_{i+1/2,j}$$
$$=\frac{(1-\alpha)}{2\Delta x}u^n_{i+1/2,j}(u^n_{i+3/2,j}-u^n_{i-1/2,j})$$
$$+\frac{\alpha}{2\Delta x}[(u^n_{i+3/2,j}-u^n_{i+1/2,j})(u^n_{i+1/2,j}-|u^n_{i+1/2,j}|)$$
$$+(u^n_{i+1/2,j}-u^n_{i-1/2,j})(u^n_{i+1/2,j}+|u^n_{i+1/2,j}|)]$$

$$FUY=\left(v\frac{\partial u}{\partial y}\right)^n_{i+1/2,j}$$
$$=\frac{(1-\alpha)}{2\Delta y}v^n_{i+1/2,j}(u^n_{i+1/2,j+1}-u^n_{i-1/2,j-1})$$
$$+\frac{\alpha}{2\Delta y}[(u^n_{i+1/2,j+1}-u^n_{i+1/2,j})(v^n_{i+1/2,j}-|v^n_{i+1/2,j}|)$$
$$+(u^n_{i+1/2,j}-u^n_{i+1/2,j-1})(v^n_{i+1/2,j}+|v^n_{i+1/2,j}|)]$$

$$v^n_{i+1/2,j}=0.25(v^n_{i+1,j+1/2}+v^n_{i+1,j-1/2}+v^n_{ij+1/2}+v^n_{ij-1/2})$$

and

$$(\tau_{xx})^n_{i+1,j}=\tfrac{2}{3}\mu^n_{i+1,j}\left[\frac{2}{\Delta x}(u^n_{i+3/2,j}-u^n_{i+1/2,j})\right.$$
$$\left.-\frac{1}{\Delta y}(v^n_{i+1,j+1/2}-v^n_{i+1,j-1/2})\right]$$

$$(\tau_{xx})^n_{ij}=\tfrac{2}{3}\mu^n_{ij}\left[\frac{2}{\Delta x}(u^n_{i+1/2,j}-u^n_{i-1/2,j})\right.$$
$$\left.-\frac{1}{\Delta y}(v^n_{ij+1/2}-v^n_{ij-1/2})\right]$$

$$(\tau_{xy})^n_{i+1,j+1/2}=\mu^n_{i+1,j+1/2}\left[\frac{1}{\Delta y}(u^n_{i+1/2,j+1}-u^n_{i+1/2,j})\right.$$
$$\left.+\frac{1}{\Delta x}(v^n_{i+1,j+1/2}-v^n_{ij+1/2})\right]$$

$$(\tau_{xy})^n_{i+1,j-1/2}=\mu^n_{i+1,j-1/2}\left[\frac{1}{\Delta y}(u^n_{i+1/2,j}-u^n_{i+1/2,j-1})\right.$$
$$\left.+\frac{1}{\Delta x}(v^n_{i+1,j-1/2}-v^n_{ij-1/2})\right]$$

and

$$\mu^n_{i+1,j+1/2}=\tfrac{1}{4}(\mu^n_{i+1,j+1}+\mu^n_{i+1,j}+\mu^n_{ij+1}+\mu^n_{ij})$$
$$\mu^n_{i+1,j-1/2}=\tfrac{1}{4}(\mu^n_{i+1,j}+\mu^n_{i+1,j-1}+\mu^n_{ij}+\mu^n_{ij-1}).$$

Table 1. Propellant data

Simplified chemical formula of SD 1156	$C_{22}H_{29}O_{35}N_9$	from ref. [34]
Heat of explosion	4600 kJ kg^{-1}	
Density	1610 kg m^{-3}	
Rate of combustion at 1 atm	1 mm s^{-1}	estimated from ref. [17]
Primary flame temperature at 1 atm	1340 K	from ref. [17]
Combustion products at the end of the primary flame at 1 atm	$Y_{CO} = 0.34$	$Y_{CO_2} = 0.18$
	$Y_{H_2} = 0.007$	$Y_{H_2O} = 0.14$
	$Y_{O_2} = 0$	$Y_{NO} = 0.26$
	$Y_{N_2} = 0.073$	adjusted from ref. [17]

The superscript n denotes a quantity evaluated at time $n\Delta t$, where Δt is the time step. For convenience, the superscript $n+1$ on quantities evaluated at time $(n+1)\Delta t$ is omitted.

In equation (22), the quantity $\bar{p}$ is an estimate of the advanced time pressure which is used in the momentum equations. This technique allows the limitation of the time step induced by the stability conditions associated with explicit schemes to be overcome, i.e. the Courant–Friedrichs–Levy condition,

$$\max_{i,j}\left(\frac{c_{i,j}\Delta t}{\Delta x}, \frac{c_{i,j}\Delta t}{\Delta y}\right) < 1$$

where $c_{i,j}$ is the local sound speed. So, long-lasting fire simulations may be reasonably performed.

An iterative Newton–Raphson scheme is used to compute the estimated pressure from an approximation of the equation of state (see refs. [32] and [33] for more details).

Gas temperature calculation from internal energy. Gas temperature cannot be deduced directly from internal energy defined in equation (6) since the species specific heat depends on temperature. So, after determining the species mass fractions and internal energy at time level $n+1$, the temperature is obtained from equation (6) using the following iterative scheme:

$$T^{k+1} = T^k - \frac{\Lambda(T^k) - e}{\Lambda'(T^k)}$$

where

$$\Lambda(T^k) = \sum_{s=1}^{N} Y_s\left[h_s(T^k) - \frac{RT^k}{M_s}\right]$$

$$\text{and } \Lambda'(T^k) = \sum_{s=1}^{N} Y_s\left[C_{ps}(T^k) - \frac{R}{M_s}\right]$$

and k is the iteration level. The iterations are continued until $|T^{k+1} - T^k| \leqslant \varepsilon$ where ε is a specified tolerance level. Convergence is typically achieved in 3–4 k iterations with $\varepsilon = 10^{-8}$.

4. RESULTS AND DISCUSSION

For the present calculations SD 1156, which is a standard 'hot' homogeneous propellant, is used. The physical and chemical data of SD 1156 are given in Table 1. No solid carbon is produced during its combustion. Due to the highly under-oxidized nature of the products issued from the fizz zone, the combustion of that kind of propellant in an air-filled cavity leads to significant afterburning reactions, as confirmed by experiments [14]. It must be underlined that, in its complete chemical formulation, SD 1156 contains salts of potassium as flame suppressant for rocket motors [34]. However, in our case, the amount of this additive seems to be not sufficient to have any effect on afterburning reactions [35].

The response of the enclosure is simulated for two cases which differ only from the opening condition of the safety-vent: (i) opening is permanent (Case I), (ii) opening occurs when the pressure at the safety-vent reaches a value of 1.5 atm (Case II). Table 2 lists the most important inputs for the calculations. Both simulations confirm the code capability to account for the full compressibility of the flow. They predict the development of the fire in a 2 m × 1 m rectangular enclosure (a length of 1 m is taken as unity in the z direction for plane flow) over 35 s for case I and 8 s for case II. The injection rate of the propellant products is 52 g s^{-1} with a burning surface of 0.0323 m^2. The opening surface is 0.0324 m^2. Calculations are performed on a rectangular 71 × 26 grid with mesh refinements near the walls. Finer mesh size is also used in the propellant combustion and opening zones (Fig.

Table 2. Typical input data for the calculations

Dimensions of the enclosure	2 m × 1 m
Opening position from the left side of the enclosure	from 1.9167 m to 1.9507 m
Propellant slab position from the left side of the enclosure	from 0.9838 m to 1.0162 m
Fire duration	35 s
Bursting pressure of the safety-vent	case I: permanent opening case II: 1.5 atm
Propellant data	
Mass	1.3 kg
Burning duration	25 s
Burning surface	0.0323 m^2
Numerical data	
Grid	71 × 26 node points
Time step	2.5×10^{-5} s

6). Case I takes about 6 hours per second on a Silicon Graphics Indigo computer.

Case I (permanent opening)

The behavior of the compartment fire can be described in terms of the time variation of the average gas pressure and temperature, and mass of oxygen within the enclosure (Fig. 7).

The three stages of the the compartment fire [1] can be easily identified in these figures.

(i) The growth or pre-flashover stage in which the average temperature is low and the fire is localized in the vicinity of its origin.

(ii) The fully developed or post-flashover fire, during which flames appear to fill the entire volume (from $t = 1.25$ s to $t = 25$ s). During this period, the enclosure appears to be fully involved and flames can escape through the opening.

(iii) The decay period (from $t = 25$ s), identified as that stage of the fire after the propellant has ceased to burn. During this stage, average gas pressure returns to its initial value of 1 atm, and average gas temperature falls or, failing that, becomes stabilized.

In Fig. 7(a), pressure increases considerably during the pre-flashover stage to attain a peak of 1.2 atm at $t = 1.25$ s in spite of the permanent ceiling opening. A sharp pressure fall during nearly 3 s is succeeded by a slower non-monotonic one until propellant combustion ends ($t = 25$ s). Just as the decay period begins, the average pressure goes back to the atmospheric value.

During the pre-flashover period, a sharp decrease of the O_2 amount due to afterburning reactions and oxygen outflow through the safety-vent is observed (Fig. 7(b)). The contribution of these afterburning reactions to the oxygen depletion will be discussed later. During this period, Fig. 7(c) shows a sudden temperature rise as a result of both afterburning processes and release of hot gaseous propellant combustion products. After this period mass outflow rate and afterburning decrease because it becomes harder and harder for CO and O_2 to reach the low regions where oxygen is present. Therefore, a slower temperature rise and a lower oxygen consumption occur. This phenomenon becomes more pronounced as time progresses. During the decay period, the mass of oxygen remains nearly constant and the temperature average approaches a value of 2040 K asymptotically.

Figures 8–10 show the iso-surfaces of gas temperature and O_2 mass fraction and velocity vector fields at selected times. Iso-surfaces of vorticity can be seen in Fig. 11. The vorticity is restricted to the range (-15)–(15) m s^{-2} in order to underscore the finer vortices.

As expected, in Fig. 8, afterburning reactions of the propellant's combustion products with the ambient air considerably increase temperature in the fire plume, up to 2200 K by $t = 11$ s.

During the pre-flashover period, temperature and O_2 mass fraction fields (Figs. 8 and 9) present a classic mushroom-shaped geometrical pattern which is slightly asymetric due to the opening of the safety-vent at the beginning. During this period, it is ambient fresh air that escapes from the enclosure. After this period, to the very moment the propellant ceased to burn ($t = 25$ s), the flow of the propellant combustion products is channeled from the source towards the opening. This is clearly visible in Figs. 10 and 11.

Because the opening is out of line with the axis of the compartment while the propellant slab is centered on the floor, a vertical deflection of the fire plume to the right is observed. The fire plume is also deflected to form a two-dimensional ceiling jet and is turned downwards. At each selected time of the calculation, the coincidence between the oxygen-free regions and the regions of the thermal field where afterburning occurred is clearly pointed out.

During the decay period, a natural convection-type flow occurs inside the enclosure leading to a stratified temperature field. At the last times of the decay period,

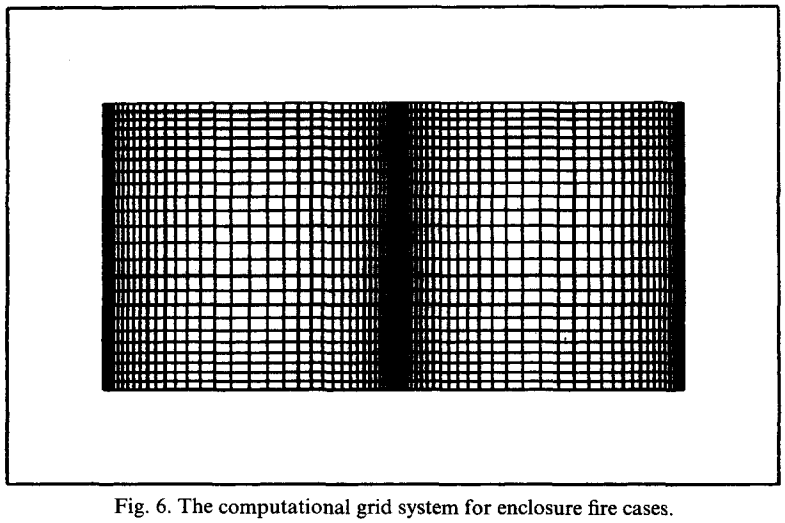

Fig. 6. The computational grid system for enclosure fire cases.

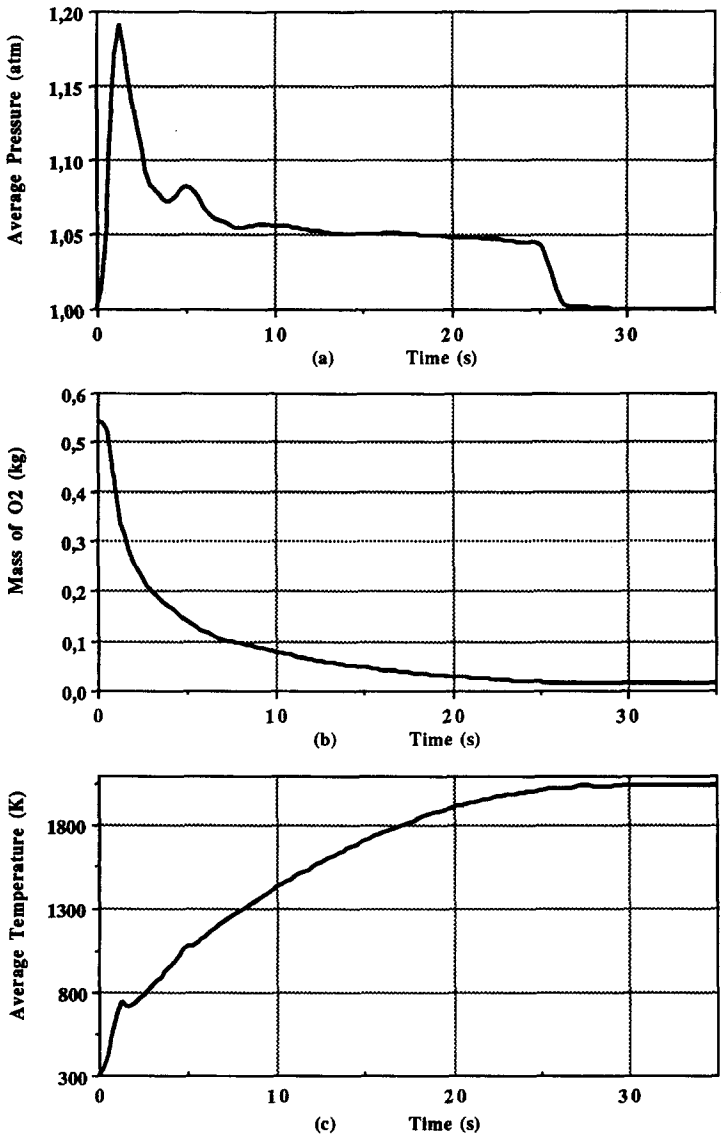

Fig. 7. Time evolution of the average gas pressure (a), mass of O_2 (b) and average gas temperature (c) in the enclosure for opening case I.

one can note the presence of a significant oxygen concentration near the opening (Fig. 9) which is due to the cold air entering the enclosure (Figs. 8 and 10).

The examination of both the velocity and vorticity fields (Figs. 10 and 11) is necessary to achieve a better understanding of the fire dynamic behaviour. As a general comment, during the entire period of the propellant combustion the vorticity field is divided into two regions on both sides of the fire plume. On the right side, the vorticity is mainly positive which corresponds to clockwise eddy while on the left side, the vorticity is mainly negative which corresponds to anticlockwise eddy. As indicated previously, the fire plume is nearly vertical in the pre-flashover stage and is deflected to the right afterwards. The reflection of the plume generates an anticlockwise eddy near the ceiling which, at $t = 3$ s, compresses the fire plume down the wall. At $t = 4$ s, this eddy is drawn outside the cavity which leads the fire plume to straighten up. The same phenomena occur also in the next two seconds, but are less pronounced due to the lower intensity of the pressure waves. Subsequently, the plume tends continuously towards the vertical position. The presence of this large anticlockwise eddy (for example, at $t = 3$ s and $t = 5$ s) makes the gas outflow more difficult which explains the non-monotonic time evolution of the average gas pressure (Fig. 7(a)). During the decay period, buoyancy forces govern the dynamic structure of the flow.

Case II (opening at 1.5 atm)

In Fig. 12, the average gas pressure, O_2 mass, and average gas temperature for case II have been superimposed on those of case I by 8 s.

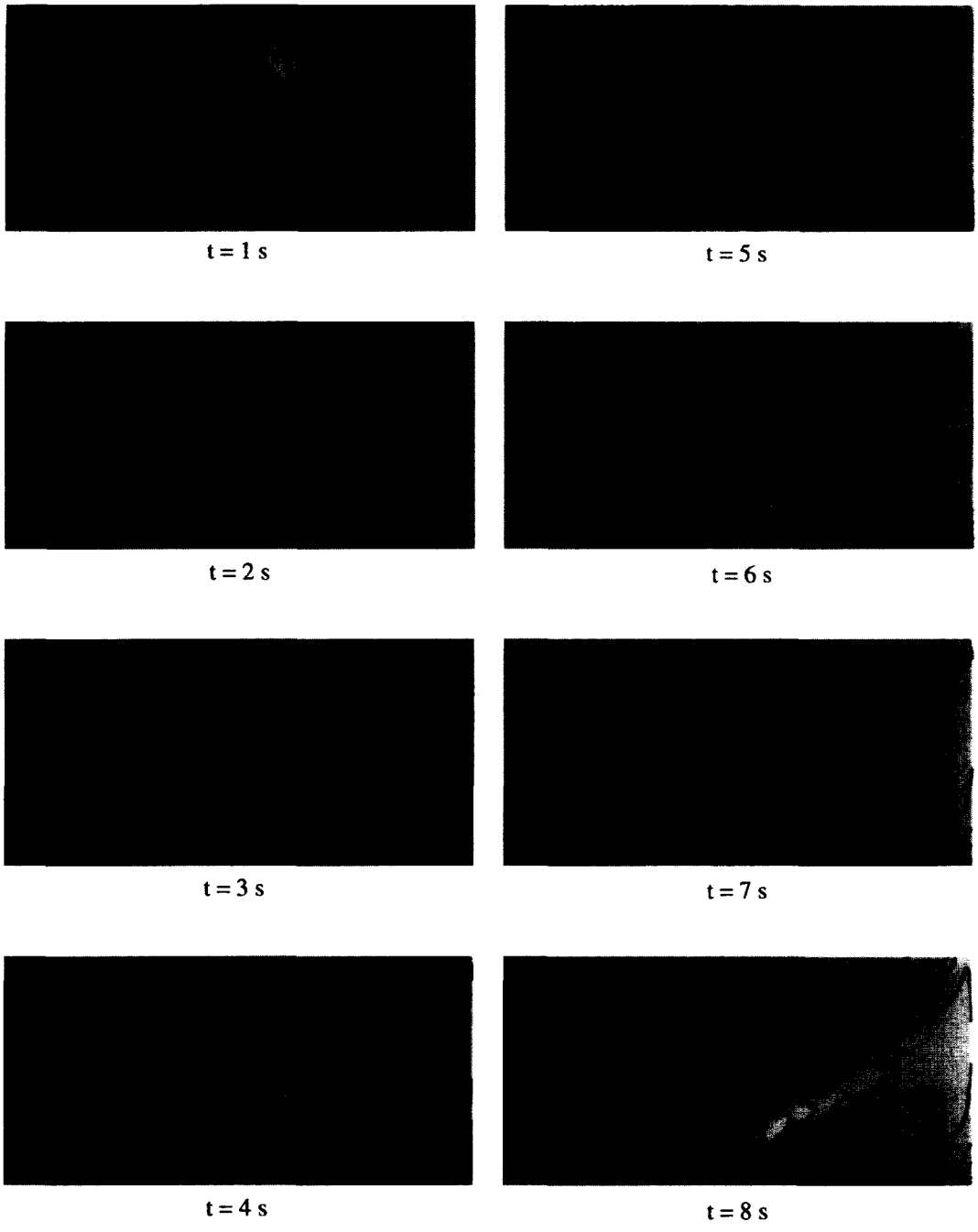

Fig. 8. Fields of gas temperature at selected times for opening case I. (*Continued opposite.*)

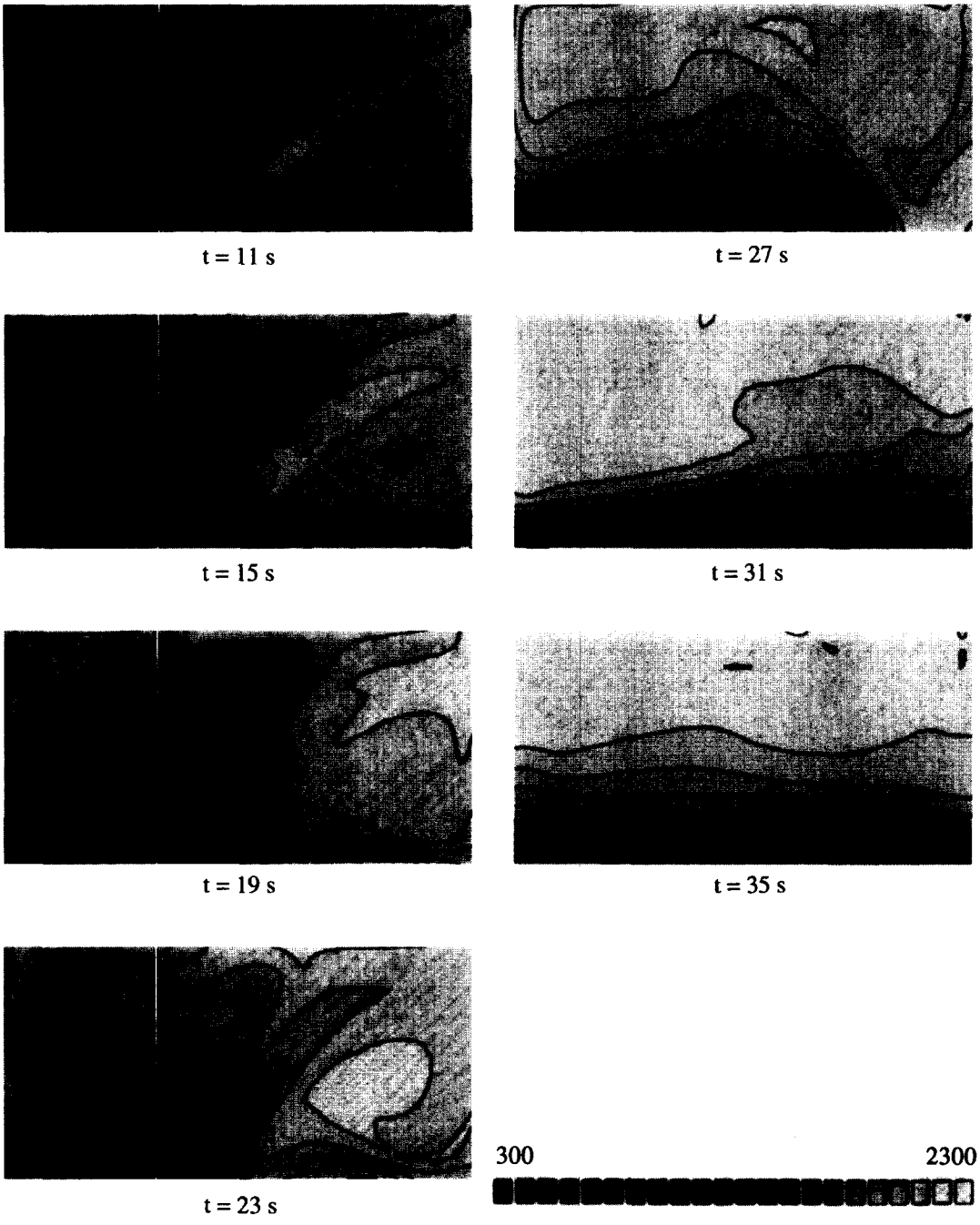

Fig. 8—*continued.*

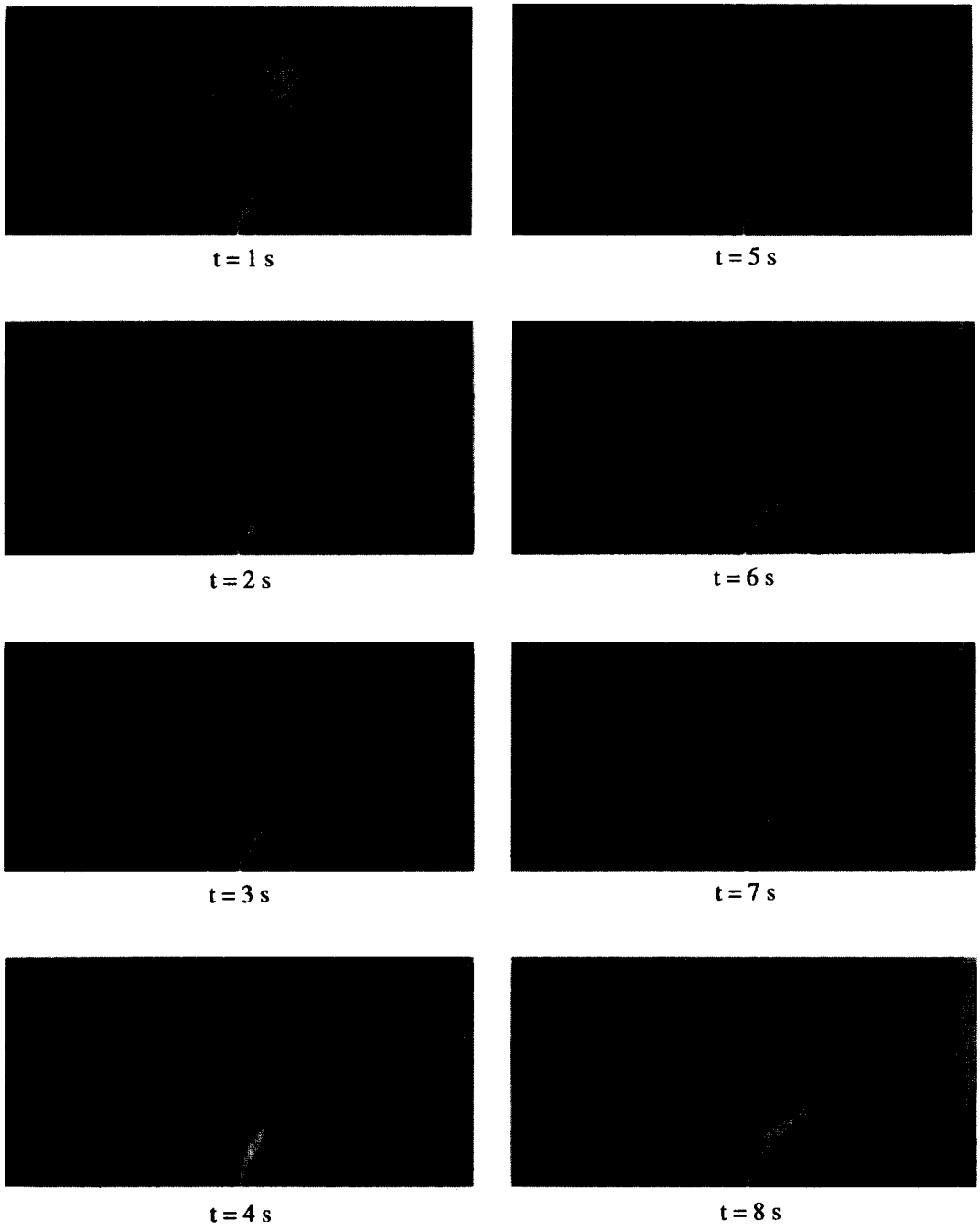

Fig. 9. Fields of oxygen mass-fraction at selected times for opening case I. (*Continued opposite.*)

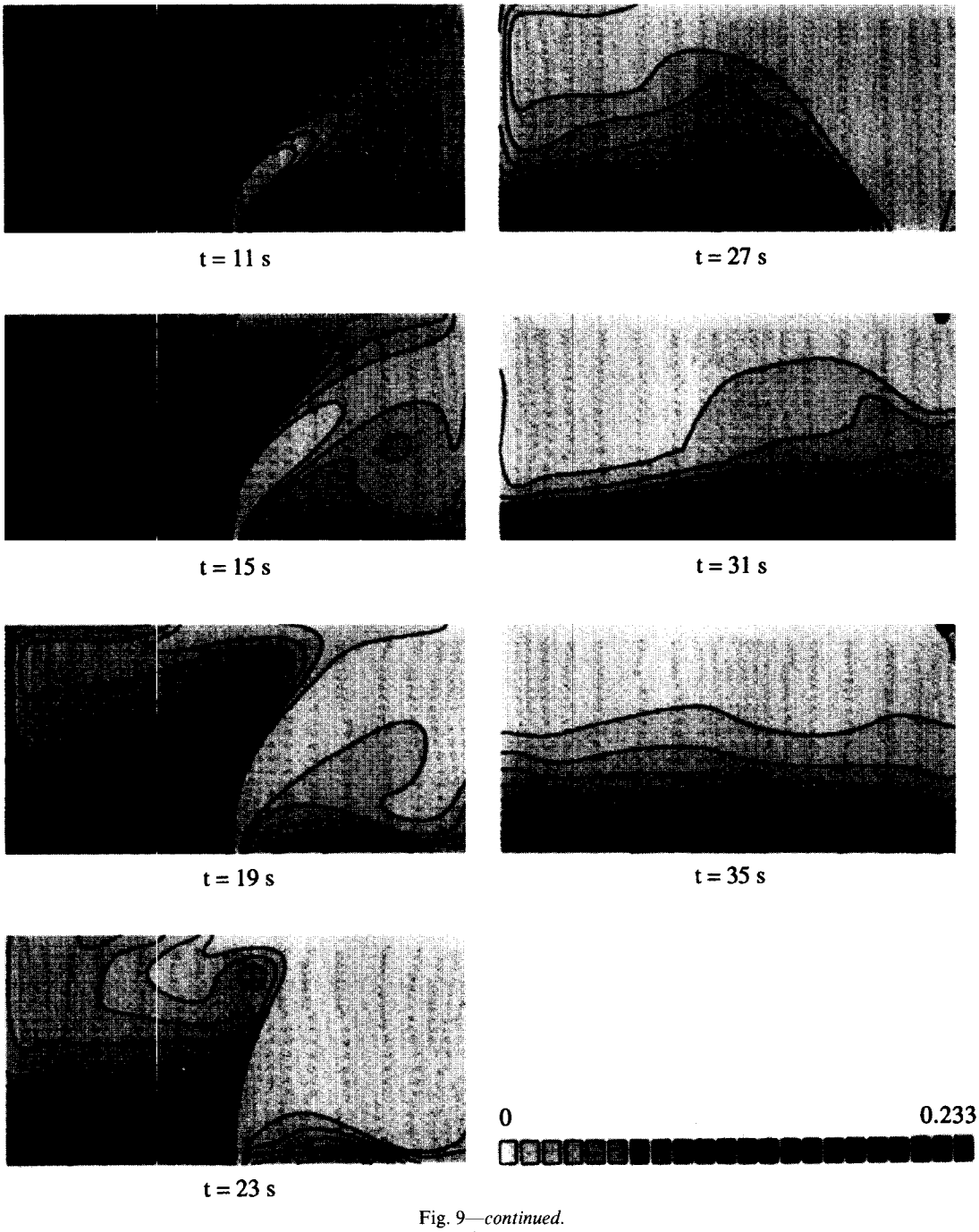

Fig. 9—*continued.*

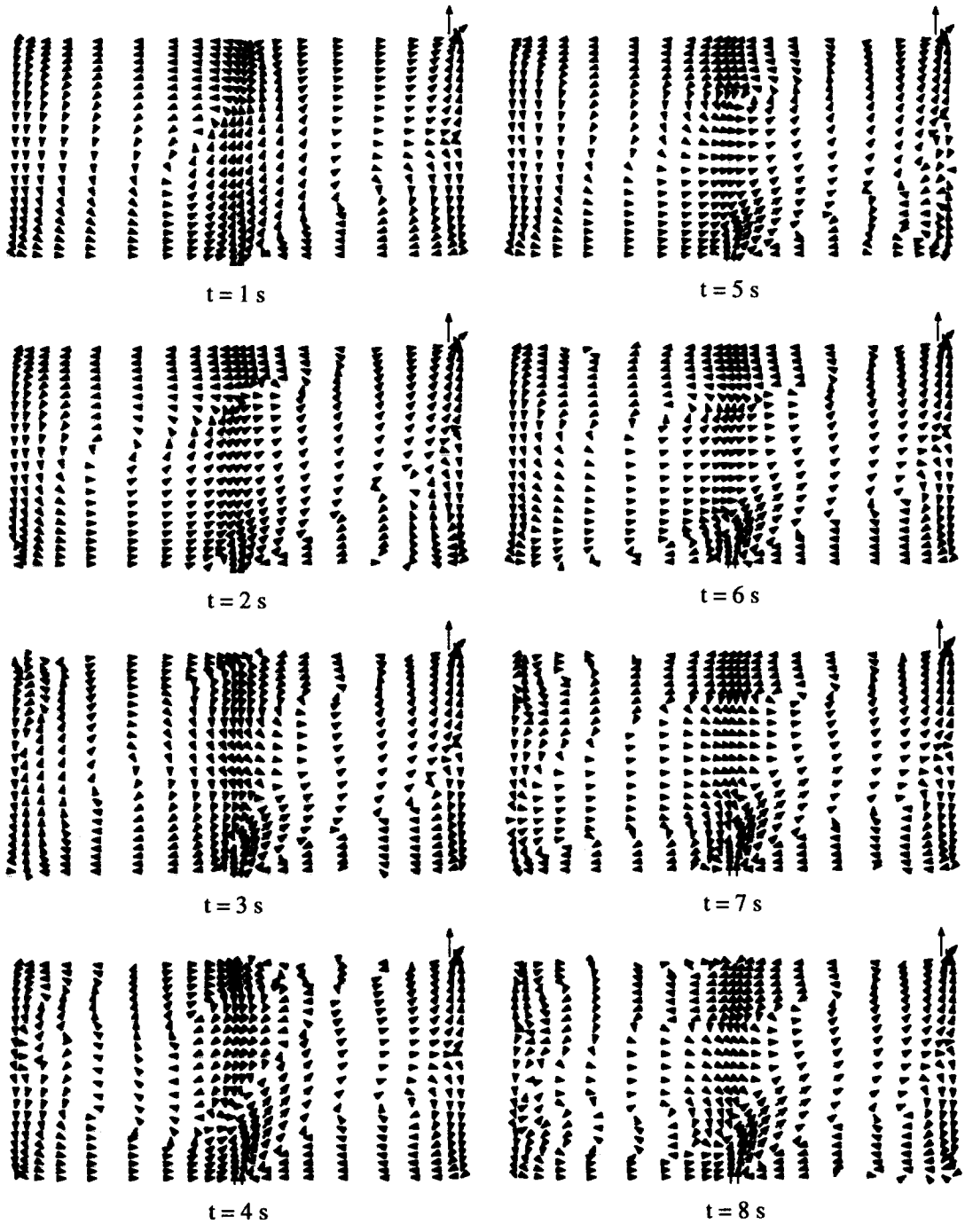

Fig. 10. Fields of velocity vector at selected times for opening case I. The largest velocity vector is in chronological order: 30.1, 27.7, 17.3, 15.1, 17.3, 14.6, 12.6, 11.7, 11.8, 11.0, 10.7, 10.1, 0.85, 0.39, 0.42 m s^{-1}. (*Continued opposite.*)

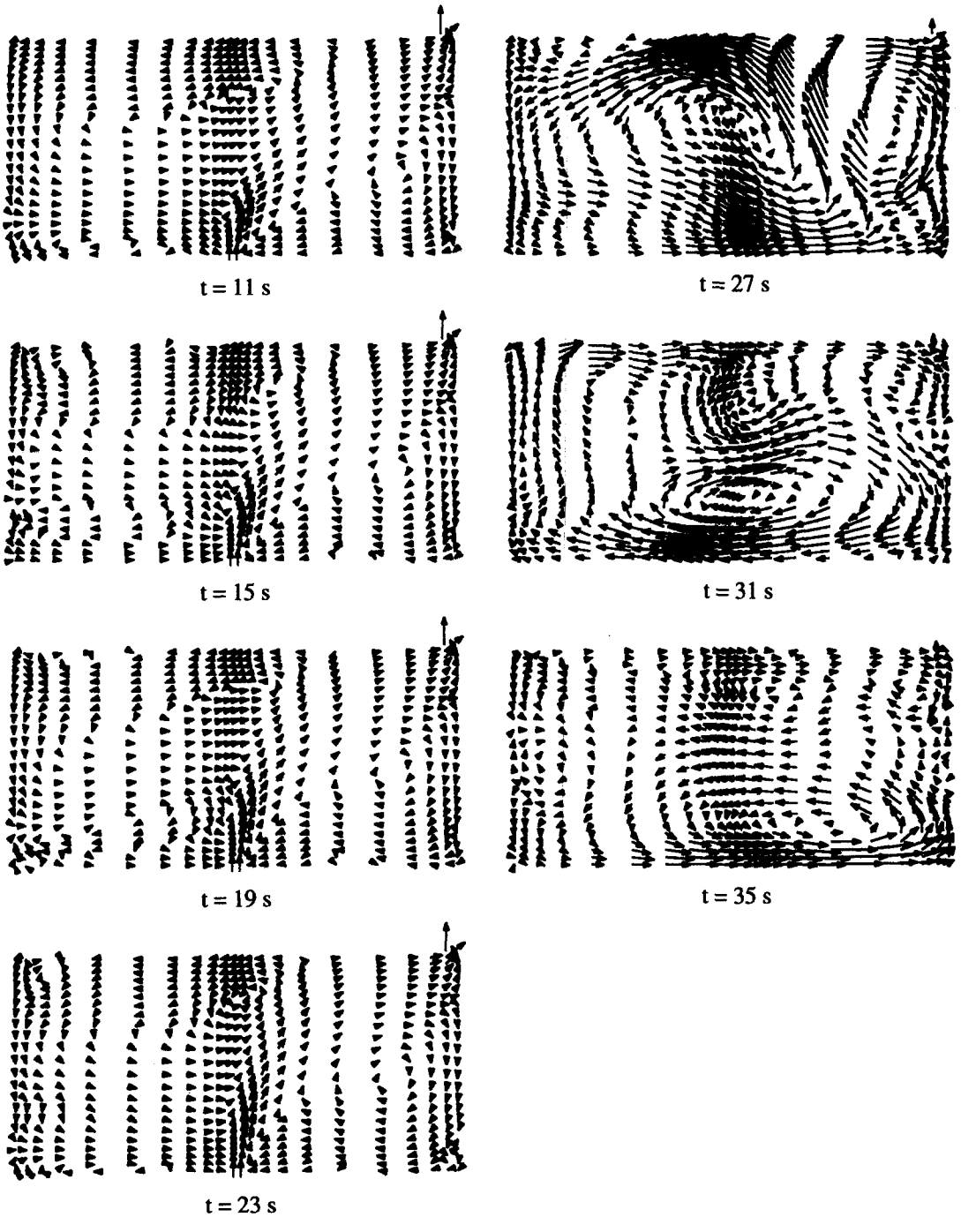

Fig. 10—*continued.*

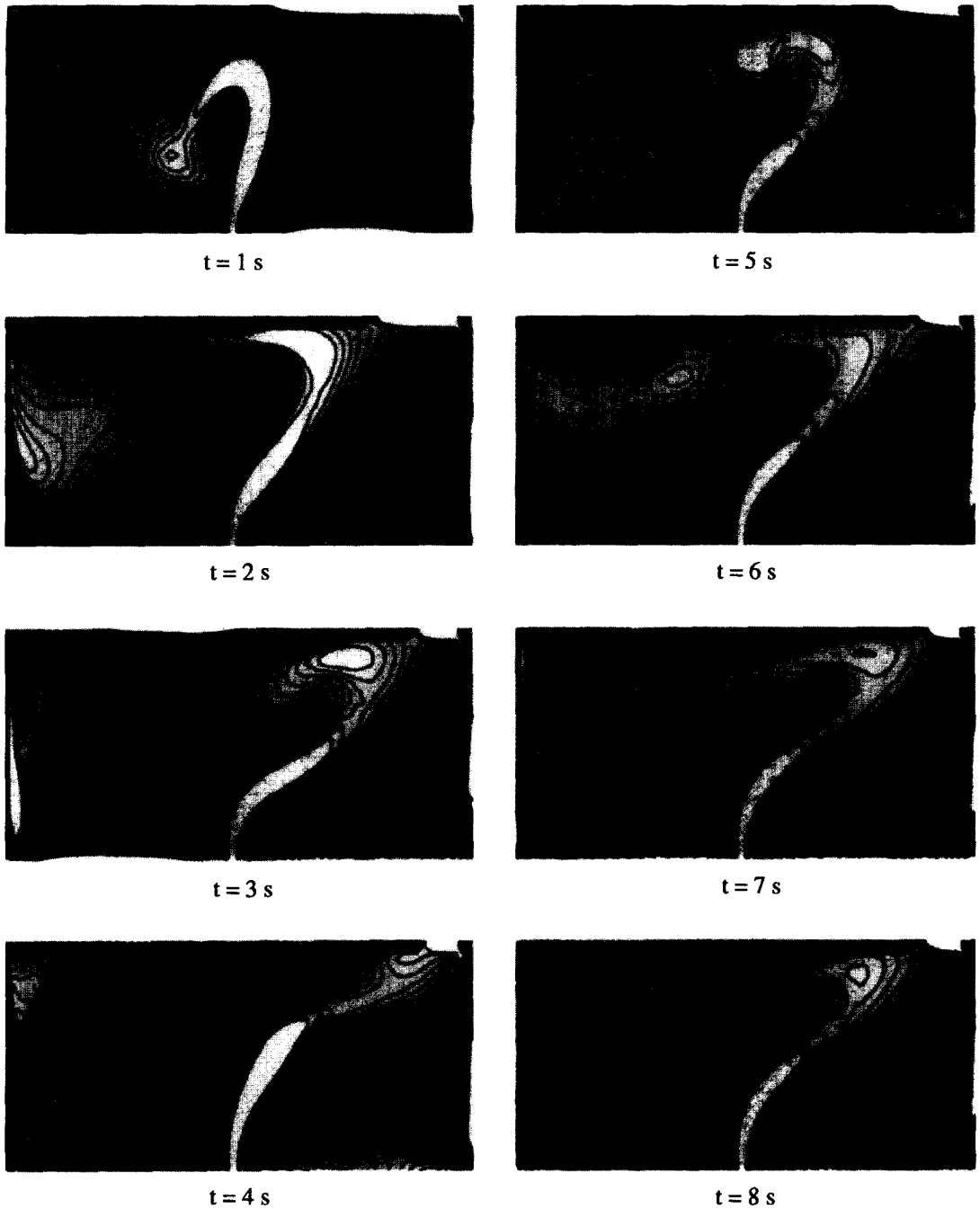

Fig. 11. Fields of vorticity at selected times for opening case I. (*Continued opposite.*)

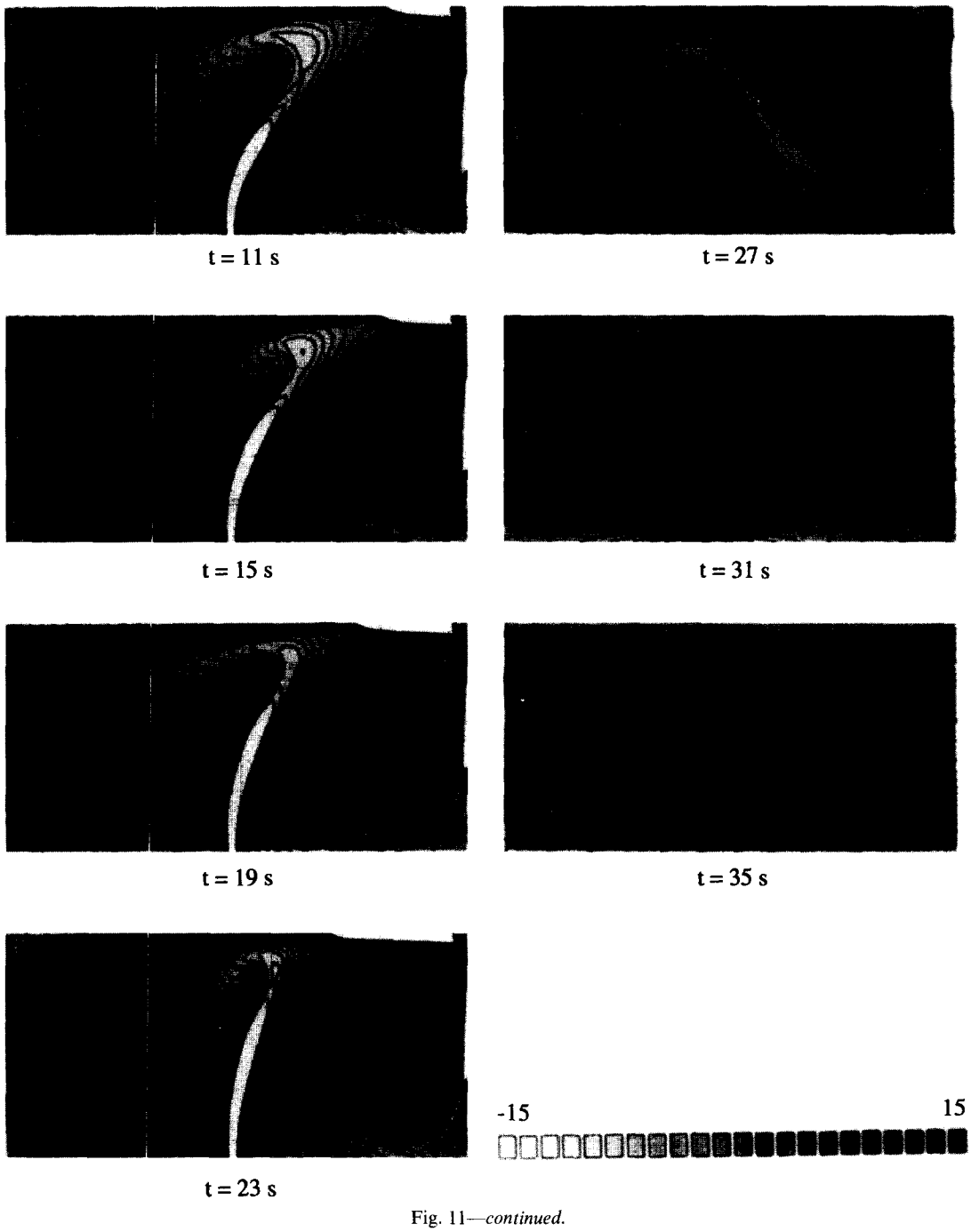

Fig. 11—*continued.*

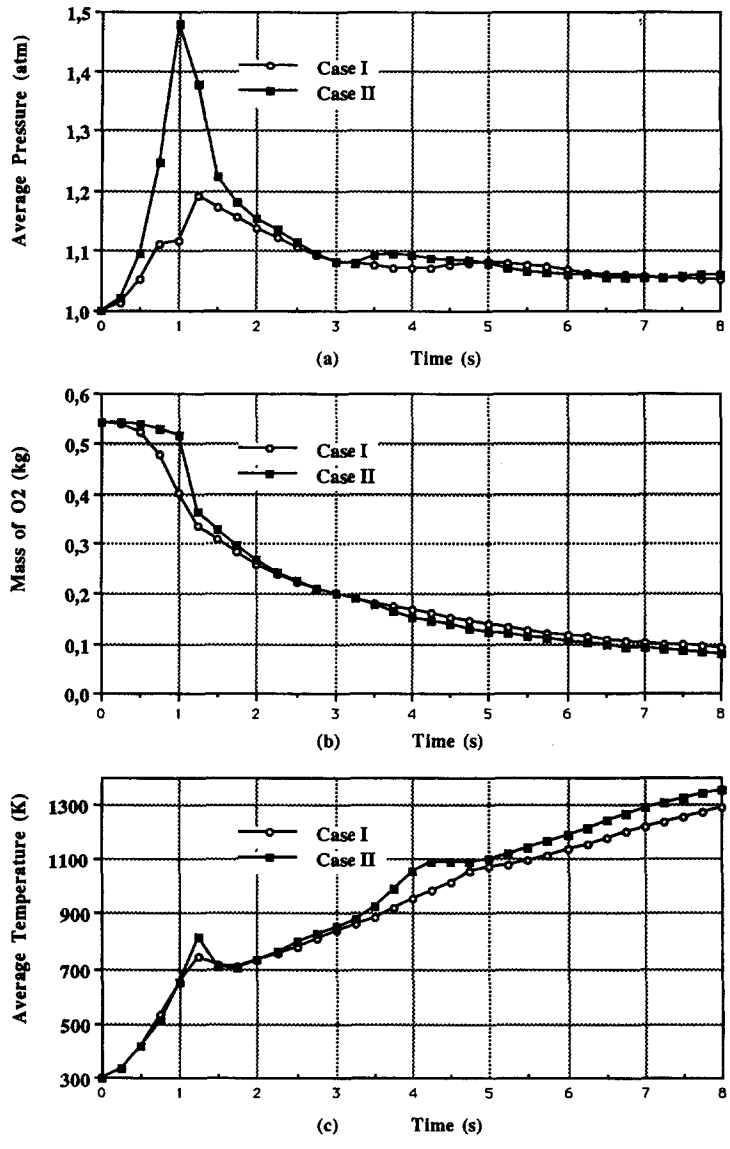

Fig. 12. Early time evolution of the average gas pressure (a), O_2 mass (b), and average gas temperature (c) in the enclosure for both opening cases.

In this case, the safety-vent opening occurs at $t = 1.018$ s for an average pressure close to the bursting pressure of the safety-vent: contrary to the first case, this seems to confirm a rapid levelling of the gas pressure at that time. Even if at past 2 s the pressure evolutions are similar, the initial reactions are quite different. Effectively, for case II, following a peak value of nearly 1.5 atm the average pressure drops quickly as a result of the sudden opening (Fig. 12(a)).

Fig. 12(b) shows for case II the occurrence of a 'plateau' effect in the evolution of the mass of oxygen by $t = 1$ s. Since there is no oxygen mass loss through the opening, it seems to indicate weak afterburning.

Concerning the average temperature as plotted on Fig. 12(c), a similar behaviour between the two cases is to be noted. The main remark is the higher temperature level in case II due to the stronger afterburning effects as proven by the higher oxygen consumption rate shown in Fig. 13(a).

Until $t = 1$ s, the low O_2 depletion rate observed in Fig. 13(a) confirms the weakness of the afterburning processes. Simultaneously, an increase of CO and H_2 masses owing to propellant combustion can be noticed

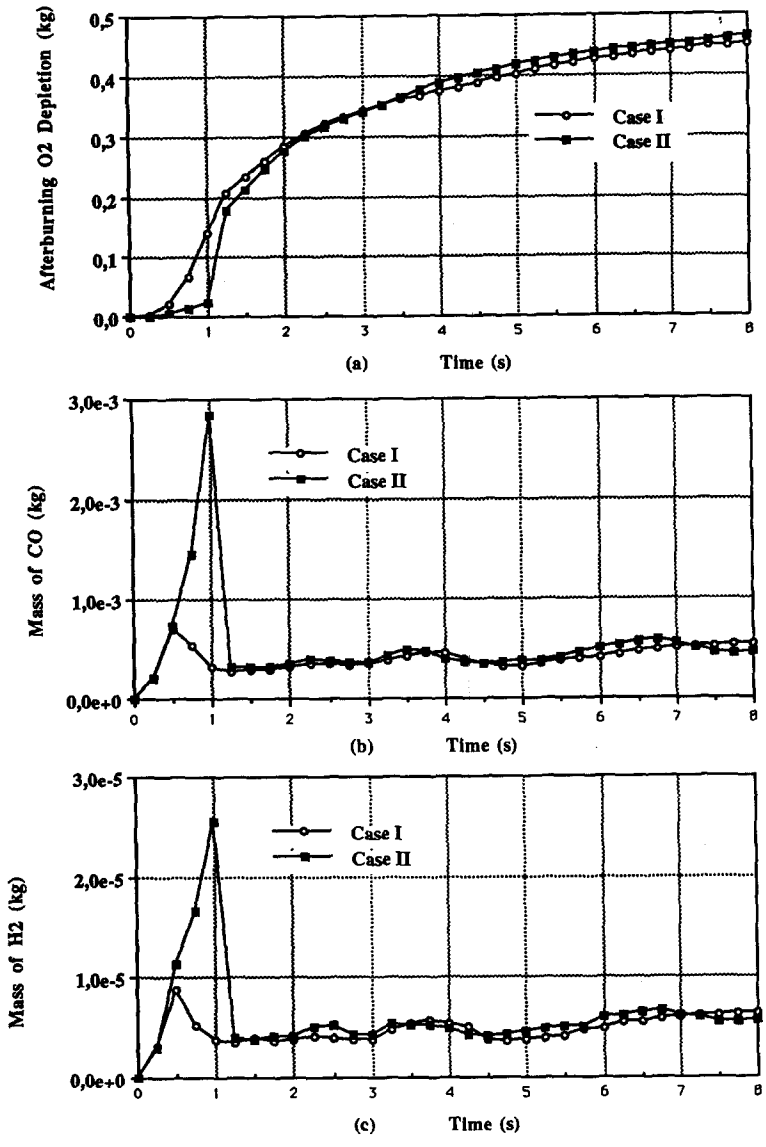

Fig. 13. Early time evolution of O_2 depletion due to afterburning reactions (a), CO mass (b) and H_2 mass (c) in the enclosure for both opening cases.

in Figs. 13(b) and 13(c). It is interesting to point out a change in slope of the H_2 mass curve at $t = 0.5$ s which explains the increase of afterburning reactions in Fig. 13(a).

From the very moment of vent opening a steep oxygen mass fall occurs (Fig. 12(b)). On the one hand, this decrease comes from oxygen outflow through the opening, and on the other hand, from afterburning reactions (Fig. 13). As time progresses, average quantities are similar for both cases.

The prediction of the gas temperature, velocity vector and vorticity fields at selected times over 8 s are shown in Figs. 14–16. As expected, inspection of the first diagram of these (corresponding to the pre-flashover period) shows that the flow is quite symmetrical about the center-line of the enclosure as the safety-vent is not yet open.

In these figures, at each selected time, it appears clearly that for case II the afterburning processes affect a larger proportion of the enclosure. This is not surprising given the greater downward penetration of the ceiling jet and the resulting negatively buoyant flow for that case. In particular at $t = 4$ s, this phenomenon induces a high inertia clockwise eddy at the lower

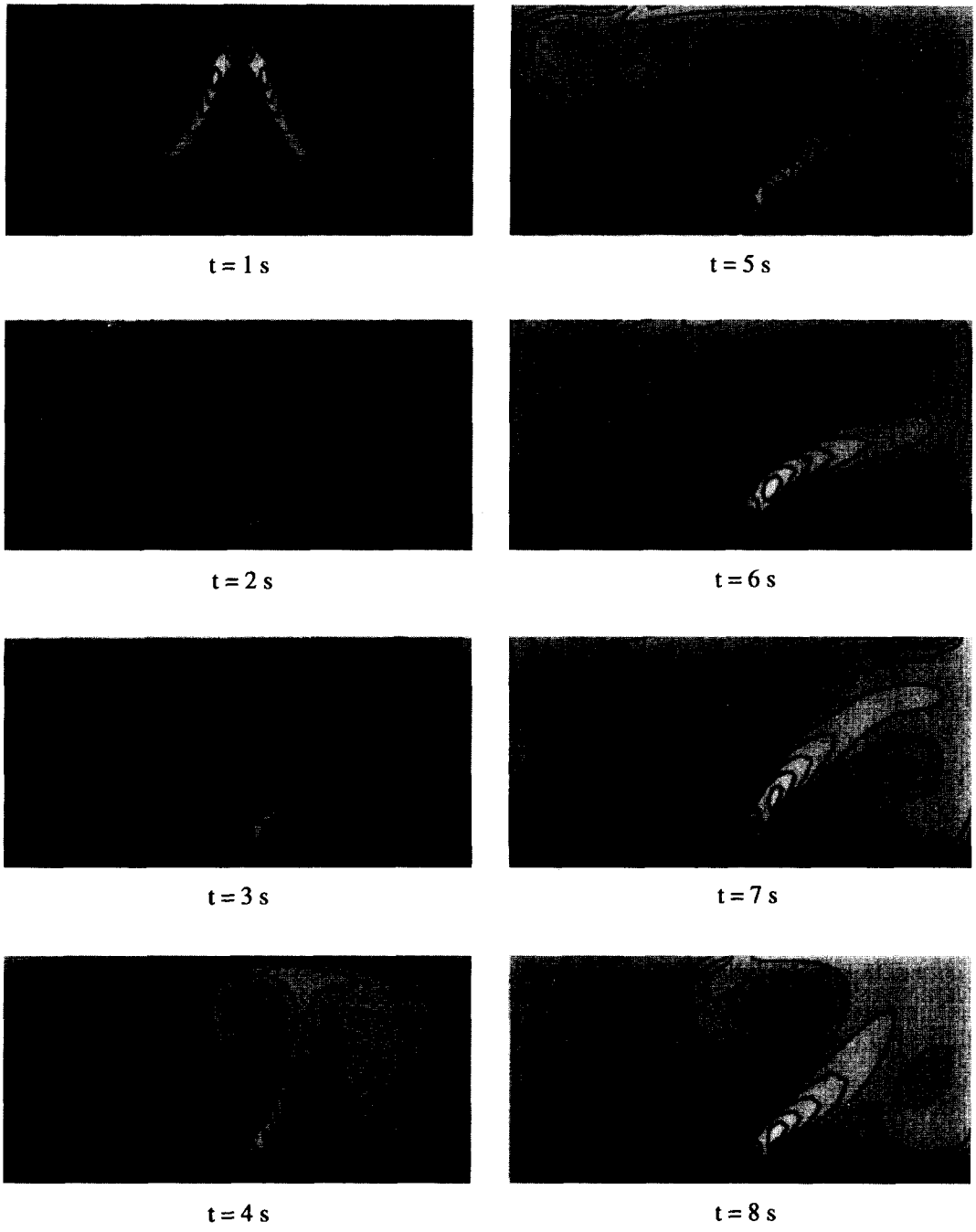

Fig. 14. Fields of gas temperature at selected times for opening case II. For convenience, the shade pattern is the same as that of Fig. 8.

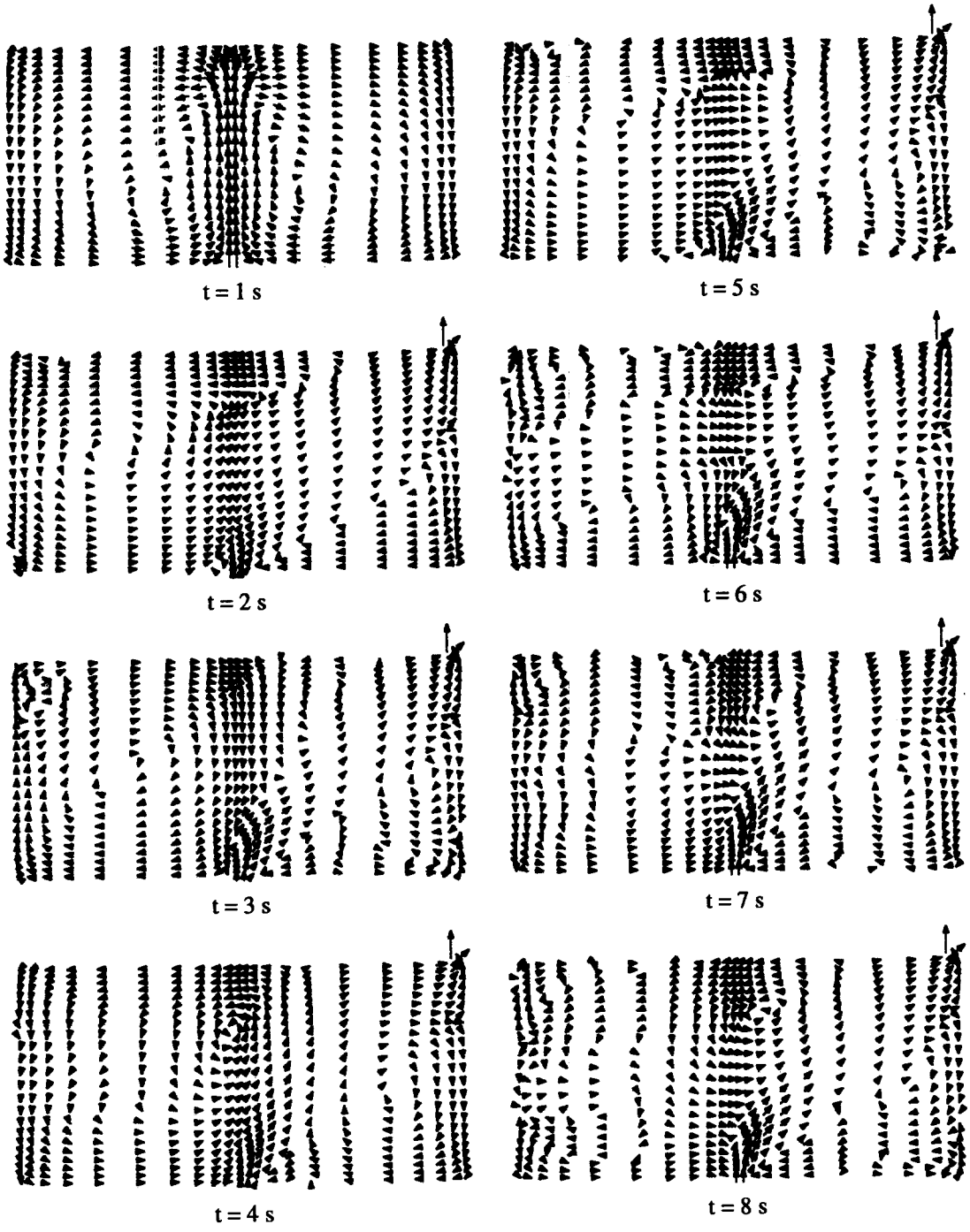

Fig. 15. Fields of velocity vector at selected times for opening case II. The largest velocity vector is in chronological order: 6.0, 30.1, 17.2, 19.0, 16.9, 13.1, 12.1, 13.0 m s^{-1}.

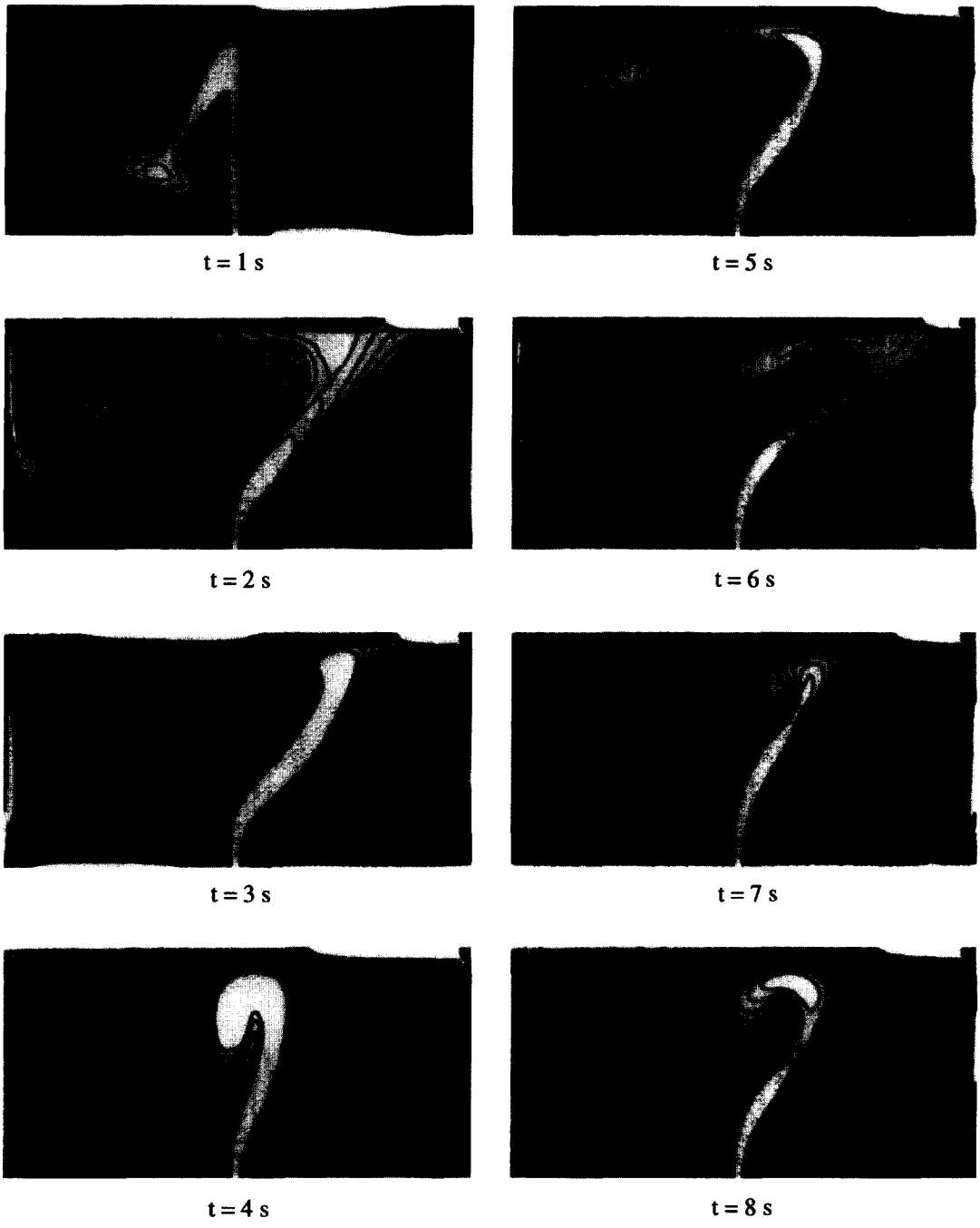

Fig. 16. Fields of vorticity at selected times for opening case II. For convenience, the shade pattern is the same as that of Fig. 11.

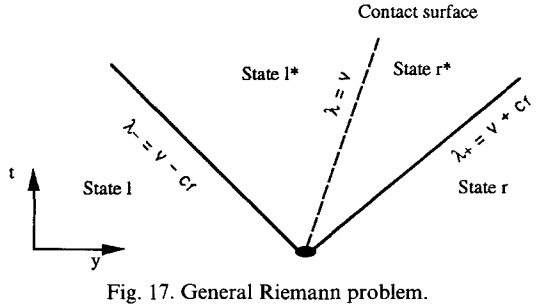

Fig. 17. General Riemann problem.

right-hand of the enclosure which has the effect of straightening up the fire plume (Figs. 15 and 16) and weakening the influence of the opening on the flow. That turns into a well-organized dynamic structure. So, two large eddies appear on both sides of the very nearly vertical plume. Subsequently, this effect persists and the fire plume seems to be less slanted for case II.

5. CONCLUSION

A mathematical model and a computer code have been developed, allowing the simulation of solid-pro-

pellant fire in a closed cavity featuring a safety-vent. It is shown that, for such fires, afterburning reactions are of primary importance. As a consequence, the average temperature level is considerably increased. Based on the examination of the time evolution of average flow quantities for two opening conditions of the safety-vent, the following remarks should be pointed out. Afterburning processes are closely linked to dynamic-induced mixing and then are greatly affected by opening conditions. In particular, in the case of delayed opening, afterburning reactions become really significant as the opening occurs.

Efficient means for propellant induced fire prevention and fighting, based upon afterburning control, are under development.

Acknowledgements—This work is supported by the CSTN/MDTC, Direction des Constructions Navales, Direction Generale de l'Armement. The authors would like to acknowledge the useful discussion that we have had with Guy Lengellé, ONERA, Paris. They are also indebted to Professor Pierre Joulain, Lab. de Chimie Physique de la Combustion, Poitiers, for his enlightening comments and suggestions.

REFERENCES

1. D. Drysdale, *An Introduction to Fire Dynamics*. Wiley, New-York (1985).
2. H. E. Mitler, Mathematical modeling of enclosure fires. In *Numerical Approaches to Combustion Modeling, AIAA Progress in Astronautics and Aeronautics* (Edited by E. S. Oran and J. P. Boris), Vol. 135, pp. 711–753 (1991).
3. H. W. Emmons, Prediction of fires in buildings, *Proceedings 17th Symposium on Combustion*, The Combustion Institute, pp. 1101–1112 (1978).
4. H. W. Emmons, The calculation of a fire in a large building, *J. Heat Transfer*, **105,** 151–158 (1983).
5. H. E. Mitler, The Harvard fire model, *Fire Safety J.* **9,** 7–16 (1985).
6. W. W. Jones, A multicompartment model for the spread of fire, smoke, and toxic gases, *Fire Safety J.* **9,** 55–79 (1985).
7. S. R. Bishop, P. G. Holborn, A. N. Beard and D. D. Drysdale, Nonlinear dynamics of flashover in compartment fires, *Fire Safety J.* **21,** 11–45 (1993).
8. G. Cox and S. Kumar, Field modelling of fire in forced ventilated enclosures, *Comb. Sci. Technol.* **52,** 7–23 (1987).
9. W. K. Chow and W. M. Leung, Solid-wall boundary effect on a building fire field model, *Combust. Sci. Technol.* **71,** 77–93 (1990).
10. Summary of damage and assessment. Report on FF G7 Class design review (October 1987).
11. J. T. Leonard, C. R. Fulper, R. L. Darwin, G. G. Back and J. L. Scheffey, Post-Flashover Fires in Simulated Shipboard Compartments—Phase 1. Small Scale Studies-Naval Research Lab. of Washington-Memorandum Report 6886 (September 1991).
12. K. Farmer *et al.*, Quantification of the Thermal Environments Generated by Combustion of Solid Rocket Propellant in Shipboard Compartments. Naval Weapons Center TP 7178 (in publication).
13. J. T. Leonard *et al.*, Project HUVUL: Propellant Fires in Shipboard Compartment. Naval Research Lab. (in publication).
14. C. Bouquet, Caractérisation de l'agression thermique générée par un incendie de propergol. Special Report 4108 CTSN/MDTC-NT/DR/93, DCN, DGA (1993).
15. A. Davenas, *Technologie des Propergols Solides*, Masson, Paris (1989).
16. N. Kubota, Survey of rocket propellants and their combustion characteristics. In *Progress in Astronautics and Aeronautics* (Edited by K. K. Kuo and M. Summerfield), Vol. 90, AIAA, New-York (1984).
17. G. Lengelle, A. Bizot, J. Duterque and J. F. Trubert, Solid propellant steady combustion-physical aspects, *AGARD, Lect. Series* **180,** 3.1–3.25 (1991).
18. G. Lengelle, A. Bizot, J. Duterque and J. F. Trubert, Steady-state burning of homogeneous propellants. In *Progress in Astronautics and Aeronautics* (Edited by K. K. Kuo and M. Summerfield), Vol. 90, AIAA, New York (1984).
19. A. Bizot and M. W. Beckstead, A model for double base propellant combustion, *Proceedings 22th Symposium on Combustion*, pp. 1827–1834. The Combustion Institute (1988).
20. M. W. Beckstead, Model for double base propellant combustion, *AIAA J.* **18,** 980–985 (1980).
21. F. A. Williams, *Combustion Theory* (2nd Edn.), Benjamin/Cummings Publishing, Menlo Park, CA (1985).
22. R. A. Fifer, Nitrate ester and nitramine propellants, In *Progress in Astronautics and Aeronautics* (Edited by K. K. Kuo and M. Summerfield), Vol. 90, AIAA, New York (1984).
23. I. Shih Tseng and V. Yang, Combustion of a double-base homogeneous propellant in a rocket motor, *Combust. Flame* **96,** 325–342 (1994).
24. O. Heuzé, H. N. Presles and P. Bauer, Computation of chemical equilibria, *J. Chem. Phys.* **83,** 4734–4737 (1985).
25. F. H. Harlow and A. A. Amsden, A numerical fluid dynamics method for all flow speeds, *J. Comput. Phys.* **8,** 197–214 (1971).
26. K. K. Kuo, *Principles of Combustion*. Wiley, New York (1986).
27. H. Guenoche and C. Sedes, Physique des Ondes de Choc. Masson, Physique Fondamentale et Appliquée (1991).
28. R. J. Kee, J. Warnatz and J. A. Miller, A Fortran computer code package for the evaluation of gas-phase viscosities, conductivities and diffusion coefficients. Sandia National Labs., Livermore, CA, Rept. SAND83-8209 (March 1983).
29. R. J. Kee, J. A. Miller and T. H. Jefferson, CHEMKIN: a general-purpose, problem-independent, transportable, Fortran chemical kinetics code package. Sandia National Labs., Livermore, CA, Rept. SAND80-8003 (March 1980).
30. C. R. Wilke, A viscosity equation for gas mixtures, *J. Chem. Phys.* **18,** 517–519 (1950).
31. D. R. Stull and H. Prophet, *JANAF Thermochemical Tables* (2nd Edn.), NSRDS-NBS37 (June 1971).
32. L. D. Cloutman, C. W. Hirt and N. C. Romero, SOLA-ICE: a numerical solution algorithm for transient compressible fluid flows. Los Alamos Scientific Lab., Los Alamos, NM, Rept. LA-6236 (July 1976).
33. L. Allançon, B. Porterie and J. C. Loraud, Etude des transferts radiatifs et convectifs induits par une source de chaleur et de masse dans une cavité à deux zones, *Int. J. Heat Mass Transfer* **36,** 3211–3227 (1993).
34. Technical Note RT 1/3384 EH, ONERA (1984).
35. Borie, ONERA, Private communication.
36. A. Jeffrey, *Quasilinear Hyperbolic Systems and Waves*. Research notes in Mathematics. Pitman Publishing (1976).
37. E. F. Toro, A fast Riemann solver with constant covolume applied to the random choice method, *Int. J. Numer. Methods Fluids* **9,** 1145–1164 (1989).
38. M. Larini, R. Saurel and J. C. Loraud, An exact Riemann solver for detonation products, *Int. J. Shock Waves* **2,** 225–236 (1992).

APPENDIX: RIEMANN PROBLEM FOR A MULTICOMPONENT FLOW

A1. *Introduction*

The system formed by the general equations for one-dimensional flows excluding the second-order terms and source terms becomes:

$$\frac{\partial \rho}{\partial t}+v\frac{\partial \rho}{\partial y}+\rho\frac{\partial v}{\partial y}=0$$

$$\frac{\partial v}{\partial t}+v\frac{\partial v}{\partial y}+\frac{1}{\rho}\frac{\partial p}{\partial y}=0$$

$$\frac{\partial e}{\partial t}+v\frac{\partial e}{\partial y}+\frac{p}{\rho}\frac{\partial v}{\partial y}=0$$

$$\frac{\partial Y_s}{\partial t}+v\frac{\partial Y_s}{\partial y}=0 \quad s=1,2,\ldots,N.$$

According to equations (6) and (7), the equation of state (EOS) can be written as:

$$\frac{p}{\rho}=Z(Y_s,T)[e-q(Y_s)]$$

with

$$Z(Y_s,T)=\frac{R\sum_{s=1}^{N}\frac{Y_s}{M_s}}{\frac{1}{T}\sum_{s=1}^{N}Y_s\int_0^T C_{ps}(T)\,\mathrm{d}T-R\sum_{s=1}^{N}\frac{Y_s}{M_s}}$$

$$\text{and}\quad q(Y_s)=\sum_{s=1}^{N}Y_s\Delta h_{fs}^0. \tag{A1}$$

Using the EOS to eliminate the pressure in the above system, it then becomes for N species in matrix form:

$$(\mathbf{I})\frac{\partial \mathbf{X}}{\partial t}+(\mathbf{A})\frac{\partial \mathbf{X}}{\partial y}=0$$

where (I) is the unit matrix

$$\mathbf{X}=(\rho,v,e,Y_1,Y_2,\ldots,Y_N)^t$$

$$(\mathbf{A})=\begin{bmatrix} v & \rho & 0 & 0 & \cdots & 0 \\ \frac{1}{\rho}\frac{\partial p}{\partial \rho} & v & \frac{1}{\rho}\frac{\partial p}{\partial e} & \frac{1}{\rho}\frac{\partial p}{\partial Y_1} & \cdots & \frac{1}{\rho}\frac{\partial p}{\partial Y_N} \\ 0 & \frac{p}{\rho} & v & 0 & \cdots & 0 \\ 0 & 0 & 0 & v & \cdots & 0 \\ \cdot & \cdot & \cdot & \cdot & \cdots & \cdot \\ \cdot & \cdot & \cdot & \cdot & \cdots & \cdot \\ \cdot & \cdot & \cdot & \cdot & \cdots & \cdot \\ 0 & 0 & 0 & 0 & \cdots & v \end{bmatrix}$$

A2. *Eigenvalues, eigenvectors*

This system allows for $N+3$ eigenvalues which are the λ solutions of the equation:

$$\det[(\mathbf{A})-\lambda(\mathbf{I})]=0$$

that is:

$$(v-\lambda)^{N+1}[(v-\lambda)^2-c_f^2]=0$$

where c_f is the frozen speed of sound in the reactive mixture given by:

$$c_f^2=\left(\frac{\partial p}{\partial \rho}\right)_{s,Y_1,Y_2,\ldots,Y_N}=\frac{p}{\rho^2}\left(\frac{\partial p}{\partial e}\right)_{\rho,Y_1,Y_2,\ldots,Y_N}+\left(\frac{\partial p}{\partial \rho}\right)_{e,Y_1,Y_2,\ldots,Y_N}.$$

The $N+3$ eigenvalues are:

$$\lambda_+=v+c_f$$

$$\lambda_-=v-c_f$$

$$\lambda=\lambda_1=\lambda_2=\ldots=\lambda_N=v.$$

Three eigenvectors are associated to the distinct eigenvalues λ_+, λ_- and λ given by:

$$\mathbf{A}\mathbf{r}_a=a\mathbf{r}_a \text{ with } a=\lambda_+,\lambda_-,\lambda.$$

They may be written as:

$$\mathbf{r}_{\lambda_+}=\left(1,\frac{c_f}{\rho},\ \frac{p}{\rho^2},\ 0,\ldots,0\right)^t,$$

$$\mathbf{r}_{\lambda_-}=\left(1,-\frac{c_f}{\rho},\ \frac{p}{\rho^2},\ 0,\ldots,0\right)^t$$

$$\mathbf{r}_{\lambda}=\left(\alpha,0,-\alpha\frac{\partial p/\partial \rho}{\partial p/\partial e}-\sum_{s=1}^{N}\gamma_s\frac{\partial p/\partial Y_s}{\partial p/\partial e},\ \gamma_1,\gamma_2,\ldots,\gamma_N\right)^t$$

where α and γ_S are arbitrary parameters.

A3. *Exact Riemann invariants*

According to Jeffrey [36], Toro [37] and Larini *et al.* [38], the equation

$$\frac{\mathrm{d}\mathbf{X}}{\mathrm{d}\sigma}=\mathbf{r}_a$$

where σ is a parameter, gives the Riemann invariants across each of the three directions λ_+, λ_- and λ. A generalization of this technique is developed for the calculation of the Riemann invariants of chemically reactive flows. They are:

Riemann invariant across direction λ_+:

$$\psi_1^{\lambda_+}=v-\int_0^{\rho}\frac{c_f}{\tilde{\rho}}(s,Y_s,\tilde{\rho})\,\mathrm{d}\tilde{\rho},\quad \psi_2^{\lambda_+}=s,$$

$$\psi_{s+2}^{\lambda_+}=Y_s(s=1,2,\ldots,N) \tag{A2}$$

Riemann invariant across direction λ_-:

$$\psi_1^{\lambda_-}=v+\int_0^{\rho}\frac{c_f}{\tilde{\rho}}(s,Y_s,\tilde{\rho})\,\mathrm{d}\tilde{\rho},\quad \psi_2^{\lambda_-}=s,$$

$$\psi_{s+2}^{\lambda_-}=Y_s(s=1,2,\ldots,N) \tag{A3}$$

Riemann invariant across direction λ:

$$\psi_1^{\lambda}=v,\psi_2^{\lambda}=p.$$

Remark. The use of the exact form of the Riemann invariants is difficult because it is necessary to calculate the integrals along isentropes and isoconcentrations in equations (A2) and (A3). It is the reason why in the present paper we are using an approximate form of the Riemann invariants. This is a good compromise in terms of both accuracy and computing time economy.

A4. *Approximate form of the Riemann invariants*

Neglecting the temperature dependence of the Z parameter when solving a Riemann problem, which assumes that C_{ps} for each species remains constant, yields:

$$c_f^2=Z(Y_s)[e-q(Y_s)][Z(Y_s)+1]$$

and the following integral may be performed analytically:

$$\int_0^{\rho} \frac{c_f}{\tilde{\rho}}(s, Y_s, \tilde{\rho})\,\mathrm{d}\tilde{\rho}$$

along a constant composition isentrope.

In these conditions the analytical relationships between states across simple waves may be obtained (see Fig. 17):

Riemann invariants across λ_+:

$$Y_{sr} = Y_{sr^*}, s_r = s_{r^*}$$

and

$$v_r = v_{r^*} - 2\left[\frac{1}{Z_r}(Z_r+1)(e_r - q_r)\right]^{1/2} \times \left[\left(\frac{p_{r^*}}{p_r}\right)^{[Z_r/2(Z_r+1)]} - 1\right] \quad \text{(A4)}$$

where $Z_r = Z(Y_{sr})$ and $q_r = q(Y_{sr})$.

Riemann invariants across λ_-:

$$Y_{sl} = Y_{sl^*}, s_l = s_{l^*}$$

and

$$v_l = v_{l^*} + 2\left[\frac{1}{Z_l}(Z_l+1)(e_l - q_l)\right]^{1/2} \times \left[\left(\frac{p_{l^*}}{p_l}\right)^{[Z_l/2(Z_l+1)]} - 1\right] \quad \text{(A5)}$$

where $Z_l = Z(Y_{sl})$ and $q_l = q(Y_{sl})$.

Riemann invariants across λ:

$$v_{r^*} = v_{l^*} = v^* \quad p_{r^*} = p_{l^*} = p^*. \quad \text{(A6)}$$

Remark. Across the λ_+ and λ_- waves the entropy is constant, thus across them the isentrope expressions are true:

$$\frac{e-q}{\rho^Z} = \text{constant} \quad \frac{e-q}{p^{Z/Z+1}} = \text{constant}$$

$$\text{and } \frac{p}{\rho^{Z+1}} = \text{constant}. \quad \text{(A7)}$$